Key Points:
- Assimilation of LPW products shows improvement on tropical cyclone (TC) prediction regardless of which parameterization scheme is applied
- TC prediction incorporating the Kain-Frish (KF) scheme shows the most improvement when LPWs are assimilated in this case
- Combining LPW assimilation with an appropriate physical parameterization scheme has a positive impact on TC prediction

Correspondence to:
T. Feng,
njuftao@126.com

Impact of Assimilating Himawari-8-Derived Layered Precipitable Water With Varying Cumulus and Microphysics Parameterization Schemes on the Simulation of Typhoon Hato

Jiazheng Lu[1,2], Tao Feng[1,2] , Jun Li[3] , Zelin Cai[1,2], Xunjian Xu[1,2], Li Li[1,2], and Jinlong Li[3]

[1]State Key Laboratory of Disaster Prevention and Reduction for Power Grid Transmission and Distribution Equipment, Changsha, China, [2]State Grid Hunan Electric Power Corporation Limited, Disaster Prevention and Reduction Center, Changsha, China, [3]Cooperative Institute for Meteorological Satellite Studies, University of Wisconsin-Madison, Madison, WI, USA

Abstract Understanding moisture information ahead of tropical cyclone (TC) convection is very important for predicting TC track, intensity, and precipitation. The advanced Himawari imager onboard the Japanese Himawari-8/-9 satellite can provide high spatial and temporal resolution moisture information. Three-layered precipitable water (LPW) with its three water vapor absorption infrared bands can be assimilated to generate better understanding and prediction of TC evolution. The impacts of LPW assimilation in the Weather Research and Forecasting model with nine combinations of physical parameterization schemes, including three cumulus parameterization (CP) and three microphysics parameterization (MP) schemes on TC prediction, have been comprehensively analyzed using Typhoon Hato as a case study. The results indicate that LPW assimilation reduces the average track error and speed up TC movement by better adjustment of the atmospheric circulation fields via changing the vertical structure of moisture and thermal profile. The track forecasts retain sensitivity to CP schemes after LPW assimilation. Also, LPW assimilation improves TC intensity prediction because the latent heat release process is accurately adjusted. It has been revealed that LPW assimilation can weaken the intensity sensitivity to MP schemes more than to CP schemes. Skill scores were used to evaluate precipitation forecasts after Hato's landfall. The results indicate that heavy precipitation forecasts are more sensitive to the choice of MP schemes. After LPW assimilation, the equitable threat scores among different results become similar and all forecast skills are increased. In addition, group statistic results with different initial time show the same conclusions.

1. Introduction

Tropical cyclones (TCs) are one of the most destructive natural disasters. Especially after landfall, a TC is often accompanied by strong winds and heavy rains that can cause considerable loss of life and damage to property (Mendelsohn et al., 2012; Mohan & Strobl, 2017). Therefore, it is important to improve the ability to predict TC track, intensity, and precipitation for disaster prevention and mitigation. The regional numerical weather prediction (NWP) model is one of the practical ways to predict TCs and study their formation, development, and dissipation. However, because TC changes rapidly, accurate prediction is still challenging. Lack of data over the ocean area, deficiencies in the parameterization of physical processes, and limited model resolution contribute to difficulties in TC prediction. Even small differences in the initial field can have a profound impact on results utilizing a variety or combinations of physical parameterization schemes (Kanase & Salvekar, 2015). Therefore, selection of a parameterization scheme and initialization is key to improve numerical prediction of TC.

Physical parameterizations play a fundamental role in determining predictive capability because they determine the crucial aspects of simulated weather (Bauer et al., 2015). These schemes represent important physical processes that cannot be directly resolved by numerical models (Stensrud, 2007). Numerous early studies concentrated on the impact of physical parameterization schemes on TC simulation. They indicated that cumulus parameterization (CP) and microphysics parameterization (MP) are two important schemes for estimating and redistributing the latent heat released by clouds from condensation and precipitation,

which is critical for sustaining large-scale disturbances in TCs (Biswas et al., 2014; Sun et al., 2015). Raju et al. (2011) demonstrated that the CP scheme primarily affects the TC intensity estimate because vertical heat distribution is more sensitivity to CP than MP. While the MP scheme affects the track estimate (since the differences in simulated tracks with different MP schemes are larger than those with different CP schemes based on analysis of Typhoon Nargis). Srinivas et al. (2012) have conducted sensitivity experiments for five TCs over the Bay of Bengal to prove that the CP scheme affects both the track and the intensity. Nasrollahi et al. (2012) showed that model outputs largely depend on the choice of MP and CP schemes but that no single combination can be considered ideal for modeling track, the time of landfall, the precipitation amount, and the areal extent.

Data assimilation is considered to be a successful approach to improving TC forecasting. In 2012, the World Meteorological Organization reported that assimilating satellite sounder observation including hyperspectral infrared (IR) and microwave data substantially improves the performance of the NWP forecast skill in predicting high-impact weather (The 5th Workshop on the Impact of Various Observing Systems on NWP in the United States, http://www.wmo.int/pages/prog/www/OSY/Meetings/Wshop-Impact-NWP-5/) compared to other meteorological observation data. Both IR and microwave sounders can provide atmospheric temperature and moisture information with high spatial resolution and have a significant effect on NWP models (Bauer et al., 2010; Cardinali, 2009; Duruisseau et al., 2017; Geer et al., 2018; Le Marshall et al., 2006; Will et al., 2009) and nowcasting (Li et al., 2011, 2012). Currently, hyperspectral IR sounders, including the Atmospheric Infrared Sounder (AIRS), the Infrared Atmospheric Sounding Interferometer (IASI), and the Cross-track Infrared Sounder (CrIS), have provided important observations that have been used to improve TC prediction (Li et al., 2016; Wang et al., 2014, 2015, 2017). Using the vertical water vapor information retrieved from an IR sounder can improve hurricane track, intensity, and precipitation estimates (Li & Liu, 2009; Liu & Li, 2010; Pu & Zhang, 2010; Zhang et al., 2016; Zheng et al., 2015). Due to the unique orbital period of polar-orbiting satellites, retrievals derived from the above-mentioned instruments onboard polar-orbiting satellites are usually available only twice a day over the same area of interest. The Advanced Baseline Imager (ABI) onboard the next generation of the Geostationary Operational Environment Satellite (GOES)-R series (Schmit et al., 2005, 2008, 2017) and the advanced Himawari imager (AHI) onboard the Japanese Himawari-8/-9 (H-8/-9; Bessho et al., 2016) provide moisture information with high spatial and temporal resolution. Assimilation with these observations has a positive effect on analysis and forecast skill in both direct and indirect ways (Ma et al., 2017). The assimilation of precipitable water developments from assimilating total precipitable water (Rakesh et al., 2009) to the three-layered precipitable water (LPW) retrieved from AHI. The results with LPW assimilation are comparable or similar to radiance assimilation (Wang et al., 2018).

To improve TC prediction, additional investigations on both physical parameterization and initialization are conducted in this study, especially when high-resolution moisture information is assimilated. The primary objective of this work is to study and understand the influence of LPW assimilation on TC prediction with different physical parameterization schemes in the Weather Research and Forecasting (WRF) model, using Typhoon Hato (2017) as an example. In this study, section 2 describes the observation data set and retrieved LPW product; section 3 provides information about the numerical model and the design of assimilation experiments; section 4 analyzes the LPW assimilation impacts on different combinations of physical parameterization schemes, followed by discussions, and a summary is contained in section 5.

2. Case Hato and Observations

2.1. Synoptic Description

Typhoon Hato was a strong and fast-moving TC that struck South China in August 2017. It first formed over the Northwest Pacific Ocean on 20 August 2017 and continuously strengthened. On 21 August, Hato emerged over the northern part of the South China Sea and attained typhoon intensity. The forward speed of Hato accelerated to 32.5 km/hr and made landfall as a super typhoon at 0450 UTC on 23 August in Zhuhai Guangdong Province, China. Thereafter, it moved westward and weakened to a tropical depression at 0600 UTC on 24 August. Typhoon Hato brought destruction to Hong Kong, Macao, and Zhuhai in China, and damage estimates on the western coast of the Pearl River were the worst in more than 50 years. The storm caused an estimated 24 deaths and more than $6.82 billion (USD) in damage. At the fiftieth annual meeting
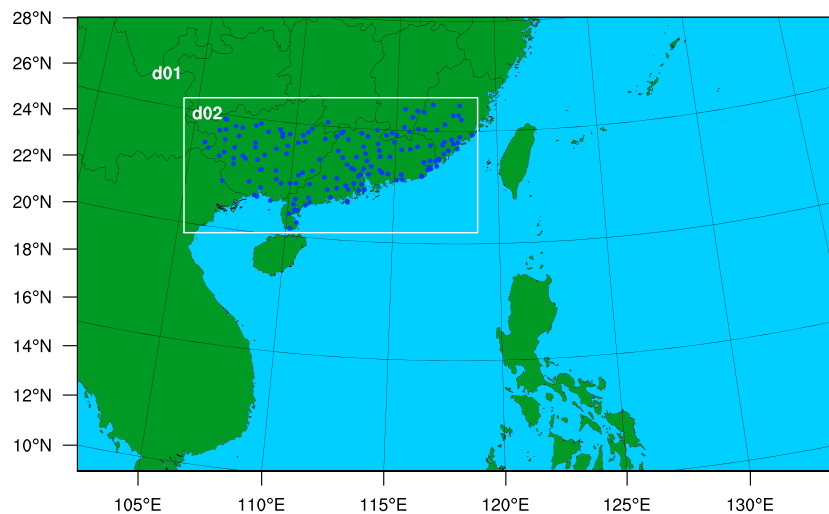
Figure 1. Configuration of the two Weather Research and Forecasting domains, named d01 and d02. Weather stations over the southeaster China are indicated by the blue dots. Rain gauge data set used in this study was obtained from these stations.

of the Economic and Social Commission for Asia and the Pacific (ESCAP) and the World Meteorological Organization Typhoon Committee, which was held in Hanoi, Vietnam, on 28 February 2018, the committee decided to retire the name of TC *Hato* due to its immense economic losses and casualties.

2.2. Ground Station Observed Precipitation

Rain gauge observations from 153 stations in South China are employed to evaluate the model-simulated precipitation (refer to Figure 1). These data are provided by the China Meteorological Administration. The stations are located across Guangdong, Guizhou, and southern Fujian Province in southern China. Since TC landfall will substantially affect the quality of the observation data, sites with missing data, errors, and abnormal observations on 23 August have been removed from this study. In order to evaluate model simulation against observation, it is typical to interpolate model output to observation locations; however, the scale mismatch will introduce a representativeness error (Tustison et al., 2001). In this study, model grid point data that are spatially close to each rain gauge location are taken as the forecast values to be compared with the corresponding observed precipitation (Efstathiou et al., 2013).

A heavy rainstorm occurred on 23 August after Hato's landfall. Using the Cressman method, the rain gauge data set is interpolated into grids and the spatial distribution of 24-hr accumulated precipitation is shown in Figure 2. The storm's center was located along the southern coast of China. The extreme value of 24-hr accumulated precipitation appeared east of Guangdong Province, and the measured value is 234.1 mm with a maximum rainfall rate of 58.6 mm/hr. Sixteen sites observed more than 100 mm of rainfall. More than 25% of the 153 sites observed precipitation that exceeds 50 mm in a 24-hr period.
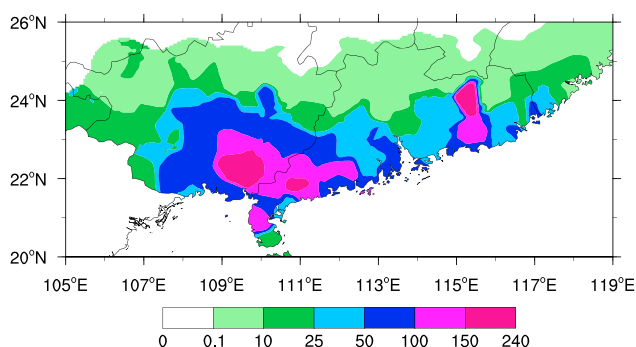
3. Three LPW Retrieved From Himawari-8 AHI Radiance Measurements

H-8 launched on 7 October 2014 in Japan; it is the first new-generation geostationary weather satellite. H-8 became operational on 7 July 2015. H-8 has a new payload, which is referred to as AHI, that captures radiances from 16 spectral bands (three visible bands, three near-IR bands, and 10 IR bands) with high temporal and spatial resolutions (Bessho et al., 2016). The coverage of H-8 spans the majority of the Western Pacific Ocean and East Asia, which renders it suitable for monitoring TCs and providing prediction information.

Figure 2. 24-hr observed accumulated precipitation (units: mm) in south China on 23 August 2017.

Table 1
The Central Wavelength of 16 AHI Bands

Band number		Central wavelength (μm)
1	Visible	0.47
2		0.51
3		0.64
4	Near infrared	0.86
5		1.6
6		2.3
7	Infrared	3.9
8*		6.2
9*		6.9
10*		7.3
11*		8.6
12		9.6
13*		10.4
14*		11.2
15*		12.3
16*		13.3

Note. The star at the right corner of band number represents the bands used for layered precipitable water retrieval.

Analysis of the 16 observation bands (Table 1) indicated that bands 8–11 and 13–16 have a close relationship with the atmospheric moisture information. Bands 8–10 are in the water vapor absorption spectral region, band 11 is used for thin ice cloud monitoring, bands 13–15 are used to monitor ice crystals/water and lower water vapor, and band 16 is used for cloud top height assignment (Bessho et al., 2016). Thus, these eight IR bands are selected for LPW retrieval.

The AHI LWP retrievals are based on the GOES-R series Legacy Atmospheric Profile (LAP) algorithm developed by the University of Wisconsin-Madison, which is a one-dimensional variational (1Dvar) retrieval method based on optimal estimation theory. The LAP algorithm consists of three steps: the first step is to identify the clear-sky pixels that are employed to calculate the AHI IR band radiances, and the second step is to derive the first guess (initial starting point X_0 for iterative solution) based on regression using the AHI IR band radiances and the Global Forecast System (GFS) short-range forecast temperature and moisture profiles as predictors. The third step is to update the first guess (X_0) to obtain the final retrieval (X_a) using the 1Dvar method with NWP as background (X_b) in the iteration (Li et al., 2000). The Quasi-Newton iteration technique is employed in the 1Dvar solution, and the University of Wisconsin-Madison's SeeBor emissivity database is applied as a known input (Seemann et al., 2008). Since the IR bands of AHI are similar to the ABI (Schmit et al., 2005), the employed bands are the same as those of the ABI. For details on the LAP algorithm, refer to the Algorithm Theoretic Basis Document (ATBD, https://www.goes-r.gov/products/ATBDs/baseline/Sounding_LAP_v2.0_no_color.pdf). Note that the LAP products have been well validated using in situ measurements (Lee et al., 2014, 2017).

After the atmospheric temperature and moisture profiles have been retrieved, the derived products (total precipitable water, three LPWs, and instability indices) are calculated from the profiles, and the methods for obtaining these products are also described in the ATBD. Following the ABI LPW process, the AHI radiances of the IR bands are averaged over clear pixels within the 5 by 5 box area for LAP retrieval, which is consistent with the current GOES Sounder LAP product (Schmit et al., 2008) with 10-km resolution at the nadir. The area can be changed to 3 by 3 (6 km) and even 1 by 1 (2 km) for future applications.

Previous studies have investigated several methods for the assimilation of satellite radiances and retrievals. Each method has advantages and disadvantages when it is used to predict TCs. Although IR radiance assimilation has been operationally and successfully utilized at many centers, Migliorini (2012) proved that sensors with more spectral channels are advantageous to assimilation of transformed retrievals. In a recent study, Wang et al. (2018) showed a positive impact from AHI radiance assimilation in predicting heavy precipitation from 19 to 20 July 2016 in Beijing. In another study, Wang, Li, et al. (2018) compared AHI radiance assimilation and LPW assimilation; they demonstrated that assimilation of the three derived LPWs yielded improved precipitation prediction.

The LPW retrieval algorithm (Jin et al., 2008; Li et al., 2000) has been validated using the enhanced Visible and Infrared Imager (SEVIRI) and the GOES Sounder (Lee et al., 2014) and applied to process AHI (Lee et al., 2017) observations at the Space Science and Engineering Center (SSEC) at the University of Wisconsin-Madison. The LPWs contain three atmospheric layers in sigma vertical coordinates, including PW_low (total PW between the surface and 0.9), PW_mid (total PW between 0.9 and 0.7), and PW_high (total PW between 0.7 and 0.3). In this study, the LPW data (Figure 3) are used to analyze the impact on Hato's track, intensity, and precipitation with different combinations of physical parameterization schemes.

4. Model and Numerical Experiment Design

4.1. Mesoscale Model

The WRF is designed for both atmospheric research and operational forecasting applications. Its Advanced Research WRF (ARW) dynamical core is an extensively employed atmospheric solver due to its fully
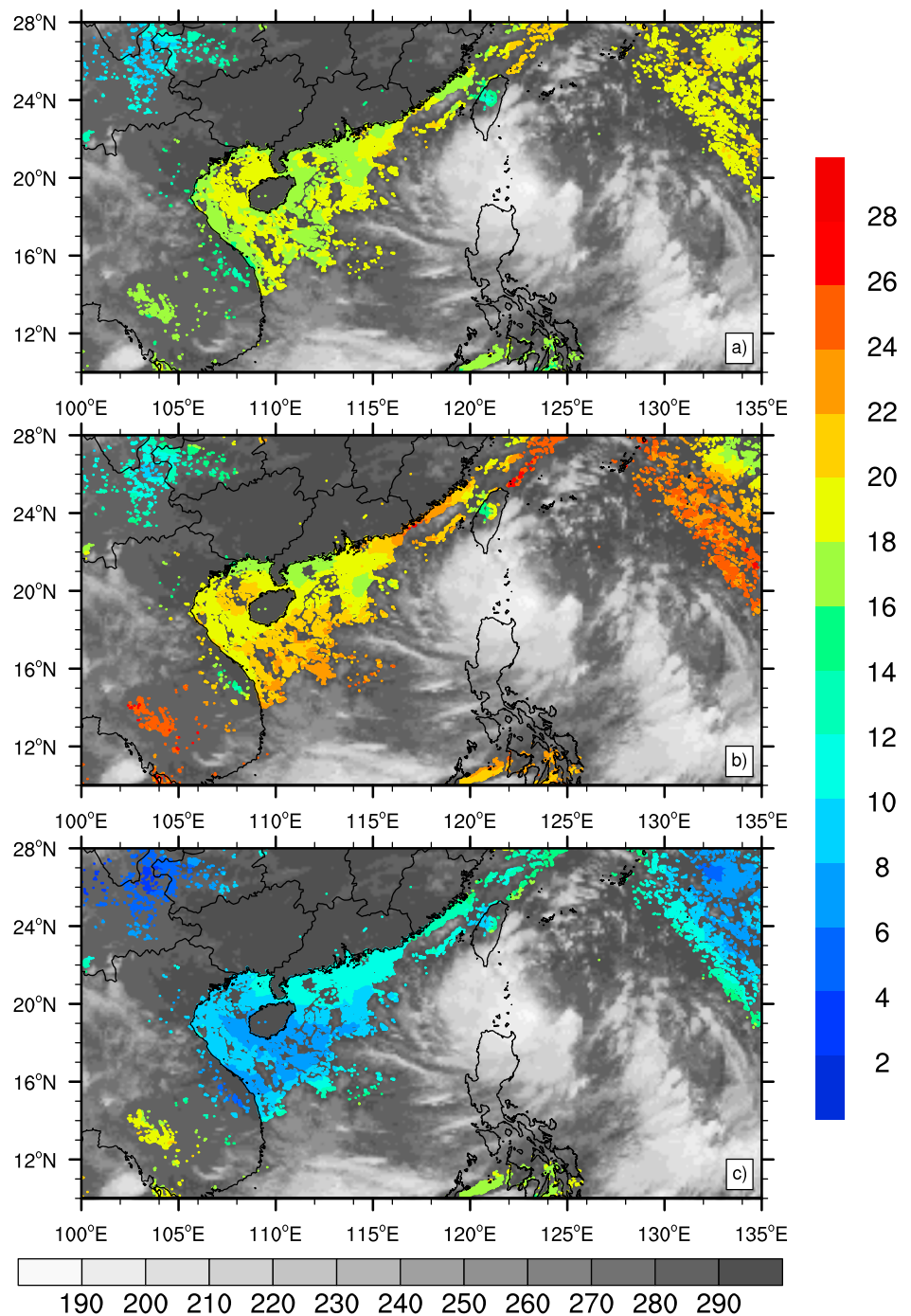
Figure 3. Retrieved three layered precipitable water (LPW): (a) PW_low, (b) PW_mid, and (c) PW_high; colored, unit: mm) overlayed on the brightness temperature of AHI channel 11.2 μm (grey, unit: K) at 0000 UTC on 21 August 2017.

compressible, primitive, nonhydrostatic Euler equations (Baldauf & Brdar, 2013). In this study, WRF-ARW version 3.5 is used. The model domain configuration, which contains one parent domain (d01) and one nested domain (d02), is shown in Figure 1. There is no feedback from d02 to d01, that is, one-way nesting. D01 covers a section of the western Pacific Ocean and southeastern China with a grid spacing of 9 km and 51 vertical levels up to 50 hPa. The model top is higher than 0.3 (upper bound of PW_high in sigma vertical coordinates), which ensures that all the three LPWs are assimilated into the model. In addition, 50 hPa is chosen as the model top in some previous studies (Biswas et al., 2014; Lin et al., 2018). D02 mainly focuses

on China's southeastern coastal region with a grid spacing of 3 km and the same vertical levels as d01. Data assimilation is conducted over d01, and d02 is generated from d01.

Cumulus convection, surface fluxes of heat, moisture, momentum, and vertical mixing in the planetary boundary layer (PBL) play important roles in the development of TC (Anthes, 1982). All processes are described by physical parameterization schemes in the NWP model. Of all physical schemes, CP and MP schemes are *physics* (Gross et al., 2018) designed to address atmospheric heat and moisture and are essential for predicting TC track, intensity, and precipitation (Nasrollahi et al., 2012). CP represents an unresolved process and is employed to formulate the statistical effect of moist convection to obtain a closed system for predicting weather (Arakawa, 2004), while MP schemes are designed for the grid-resolving scale. They are responsible for condensing and evaporating clouds, handling phase transitions within clouds, and producing precipitation from explicit clouds (Gustafson et al., 2013). CP and MP interact with each other by cloud detrainment (Fowler & Randall, 2002). The detrainment of hydrometeors (e.g., cloud ice and cloud water) from convection can enter the MP process and affect resolved scale rainfall (Song & Zhang, 2011). Assimilating LPW will adjust the initial temperature and moisture field in the whole atmosphere. Changes will directly affect the CP and MP behavior when addressing temperature and moisture (Jankov et al., 2007; Kuang, 2010; Nie & Kuang, 2012). These reactions will further affect TC prediction. Thus, CP and MP are selected for the sensitivity analysis in this study.

In the experiments, three CP and three MP schemes of the WRF model are customized for forecasting Hato. The CP scheme affects the large-scale circulation by the vertical diffusion of heat, moisture, and momentum and plays a key role in determining the vertical structure of atmospheric temperature and humidity (de Rooy et al., 2013). Three CP schemes—Kain-Frish (KF), Grell-Devenyi (GD), and no cumulus (NO) schemes—are tested in this study. The KF scheme is a deep, shallow convection subgrid scheme that use a mass flux approach with downdrafts and a convective available potential energy removal time scale (Kain, 2004). It has shown to improve results in subtropical regions when large-scale forcing is weak. The GD scheme is a cloud ensemble scheme that uses 16 ensemble members derived from five popular closure assumptions to obtain an ensemble mean realization at a given time and location (Grell & Dévényi, 2002). Based on the results of historical TC simulation in the Northwest Pacific Ocean, the KF and GD schemes are suitable choices for CP schemes (Li, 2013; Sun et al., 2014). Some studies have suggested that a CP scheme does not significantly help at fine resolution (Li & Pu, 2008). The NO scheme is an option in these experiments as well.

The MP scheme plays an important role in simulating precipitation, atmospheric heat, and sedimentation processes of hydrometers. The best choice of MP scheme varies by case. Based on previous studies, Franklin et al. (2005) demonstrated that the TC prediction was sensitive to changes in the graupel falling speed, size, and collection efficiency parameters in numerically simulated convection. Thus, the Lin scheme, WRF Single-Moment 6-class scheme (WSM6), and Thompson scheme, which include graupel, are selected for this study. The Lin scheme includes water vapor, cloud water, rain, cloud ice, snow, and graupel (Lin et al., 1983). Because more solid water variables are considered in this scheme, the process of collision between the mass variables and the new categories generated after collision are more complex. WSM6 is developed from the WRF Single-Moment 3-class scheme (WSM3) and the WRF Single-Moment 5-class scheme (WSM5). The microphysics process in WSM6 is more complex than that of the WSM5 scheme. It predicts six categories of water (Hong & Lim, 2006). Compared with the Lin scheme, the process of collision and the selection of some empirical parameters are different. The new Thompson scheme (Thom) is a double-moment scheme that considers not only ice, snow, and graupel processes but also rain and ice number concentration (Thompson et al., 2008). This scheme is an improved version of the earlier Reisner scheme (Reisner et al., 1998). The calculation of the microphysical process is more accurate because the number concentration is not calculated by empirical relation. Both the WSM6 scheme and Thom scheme are developed from the Lin scheme and are frequently used for TC prediction over the Western Pacific (Zhang & Wang, 2018).

Nine control experiments (CTRLs) are performed with different combinations of CP and MP schemes to assess the impact of LPW assimilation on physical processes. Table 2 lists the experiments' names. According to the parameterization schemes used in the simulations, the experiments are divided into six categories. KG, GG, and NG are the group names of the experiments with the same CP scheme, while LG, WG, and TG are the group names of experiments with the same MP scheme.

Table 2
Combinations of Cumulus and Microphysics Options for Different Sensitivity Analyses

Cumulus	Microphysics			Group experiments name
	Lin	WSM6	Thompson	
Kain-Fritsch	Lin-KF	WSM6-KF	Thom-KF	KG
Grell-Devenyi ensemble scheme	Lin-GD	WSM6-GD	Thom-GD	GG
No cumulus	Lin-NO	WSM6-NO	Thom-NO	NG
Group experiments name	LG	WG	TG	

Other parameterizations chosen in this study include the Yonsei University PBL scheme (Hong et al., 2006), the Rapid Radiative Transfer Model (RRTM) longwave radiation scheme (Mlawer et al., 1997), the Dudhia shortwave radiation scheme (Dudhia, 1989), and the Noah land surface scheme (Chen & Dudhia, 2001). They are used together with the selected CP and MP schemes.

4.2. Data Assimilation System

The assimilation system that is applied in this paper is the Gridpoint Statistical Interpolation (GSI) system, version 3.3. Currently, the GSI data assimilation, which is developed by the National Oceanic and Atmospheric Administration (NOAA), can be run as a data assimilation system of three-dimensional variational (3-D Var), 3-D ensemble-variational (3-D En-Var), 4-D En-Var, 3-D/4-D hybrid En-Var, or 4-D Var data assimilation system. The assimilation is operationally employed at the National Centers for Environmental Prediction. Note that 4-D hybrid En-Var GSI is currently operationally employed at NOAA and National Centers for Environmental Prediction (Shao et al., 2016). The definition of the background error covariance operator is developed from the spectral version to the grid point version, which is based on recursive filters (Parrish & Derber, 1992). The code design of GSI is more flexible and suitable for parallel computing and allows for both global and regional data assimilation capability. GSI is primarily designed to improve weather forecasts (Kleist et al., 2009; Wang et al., 2013; Wu et al., 2002). The variational analysis method utilized in the GSI is based on a given dynamic constraint, which consists of at least one atmospheric motion equations to minimize the difference between the first guess and the observed value to generate the initial field. The principle of the GSI 3D-Var is to convert the data assimilation problem into a problem that minimizes the cost function J as

$$J(X) = \frac{1}{2}[X-X_b]^{\mathrm{T}}B^{-1}[X-X_b] + \frac{1}{2}[H(X)-Y]^{\mathrm{T}}R^{-1}[H(X)-Y] \qquad (1)$$

where X is the analysis field of atmospheric state variables, X_b is the background field, B is the background error covariance, R is the observation error covariance, H is the observation operator, and Y is the observation. Thus, the 3-D Var analysis field is the solution when the objective function attains a minimum value.

The assimilation performed once at 0000 UTC on 21 August 2017, followed by a 72-hr forecast. Figure 4 shows assimilation and forecast procedures. LPW data retrieved from AHI are assimilated into CTRLs in
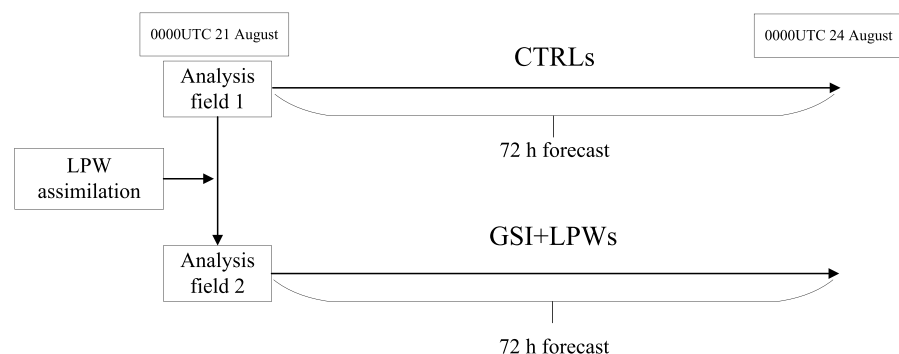

Figure 4. Assimilation and forecast procedures for both CTRLs and Gridpoint Statistical Interpolation + layered precipitable waters (GSI + LPWs).
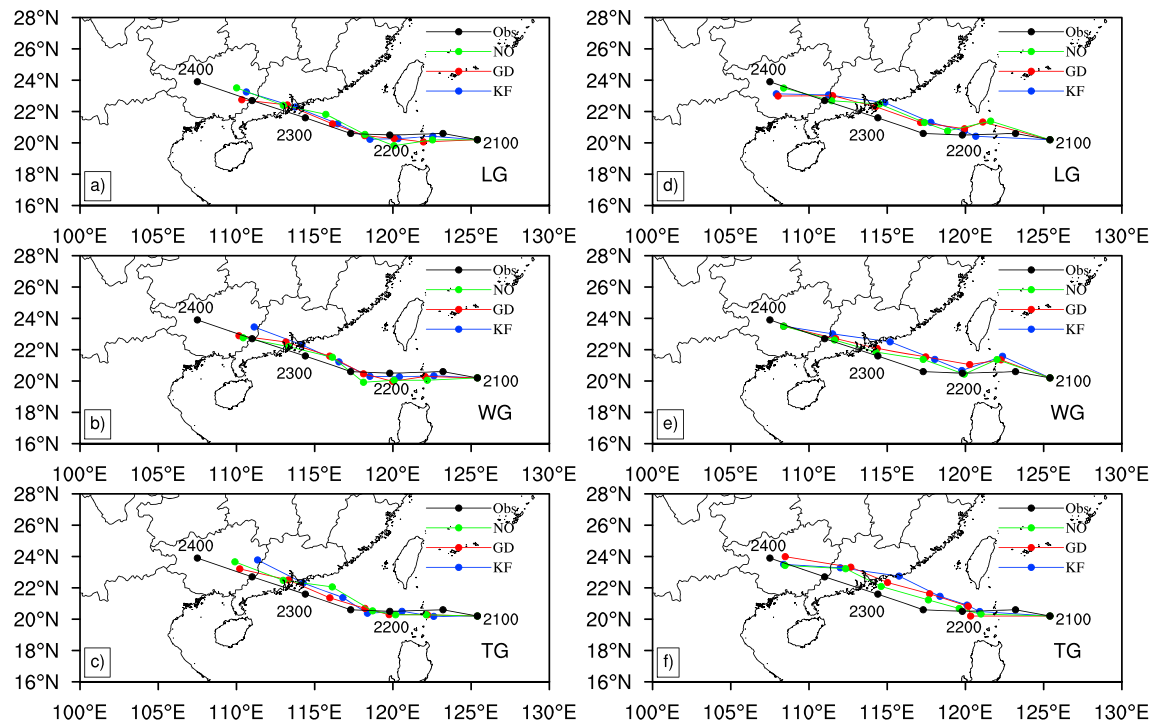
Figure 5. The 72-hr track forecast of CTRLs (left panel, (a) LG, (b) WG, and (c) TG) and assimilation with layered precipitable water (LPW; right panel, (d) LG, (e) WG, and (f) TG) from 0000 UTC on 21 to 0000 UTC on 24 August.

d01 with an NAM background error covariance matrix (GSI + LPWs). The assimilation window is 1 hr, which has a ±0.5 hr interval centered at 0000 UTC. The three LPW observation errors are set to 1.16, 1.75, and 1.22 mm for low layers, middle layers, and high layers, respectively. The slight changes in observation errors are not sensitive to the final prediction results (Wang, Liu, et al., 2018).

5. Results and Discussion

In this study, nine CTRLs and nine GSI + LPWs are conducted by the WRF and GSI assimilation system to predict Hato. All experiments were initialized at 0000 UTC on 21 August 2017. The GFS analysis filed (AF1; without LPW assimilation) at 0000 UTC 21 August 2017 was employed as the initial conditions in CTRLs. AF1 with LPW assimilation (refer as AF2) at 0000 UTC on 21 August is utilized as the initial conditions for GSI + LPWs. In addition, 72-hr forecasts from both CTRLs and GSI + LPWs begin from 0000 UTC on 21 August to 0000 UTC on 24 August 2017. No vortex initialization is conducted in the experiments since the bias of location and intensity is small. The comparisons between the forecasts (track, intensity, and precipitation) and the observations (the best estimate data from the Japan Meteorological Administration and precipitation observation from China Meteorological Administration) are preformed to analyze the effect of LPW assimilation on TC prediction and to test the sensitivity of the parameterization scheme on LPW data assimilation.

5.1. Impacts on Track Forecasts

The 72-hr forecast tracks of Typhoon Hato from CTRLs and with LPW assimilation are shown in Figure 5. The Best Track (black line) data from the Japan Meteorological Administration is used to assess the performance of forecast results with different parameterization combinations.

The tracks obtained from all CTRLs show the initial westward movement and a distinct turn to the northwest after 36 hr of integration. The predicted track errors increase with time, and the bias of 24-, 48-, and 72-hr forecasts are 23.8–81.2 km, 137.5–249.4 km, and 245.6–391.6 km, respectively in CTRLs (refer to Table 3). The track errors are significantly reduced, and the forecast results for each scheme are closer to

Table 3
The Forecast Track Error of Typhoon Hato

Name of experiments	CTRLs (km)			GSI + LPWs (km)		
	24 hr	48 hr	72 hr	24 hr	48 hr	72 hr
Lin-KF	60.8	218.3	326.9	31.0	116.9	95.3
Lin-GD	38.1	185.2	316.8	46.9	80.2	114.2
Lin-NO	80.6	137.5	259.1	102.0	98.5	100.0
WSM6-KF	68.5	226.4	372.9	19.2	128.3	100.0
WSM6-GD	61.1	161.2	293.6	78.2	53.5	100.0
WSM6-NO	57.9	179.0	324.8	14.3	30.4	100.0
Thom-KF	81.2	249.4	391.6	54.3	189.5	100.0
Thom-GD	23.8	164.6	286.6	53.2	104.2	100.1
Thom-NO	45.7	184.7	245.6	28.9	58.6	111.7
LG	59.9	180.3	300.9	59.9	98.5	103.2
WG	62.5	188.9	330.4	37.2	70.7	100.0
TG	50.2	199.5	307.9	45.4	117.4	103.9
KG	70.2	231.4	363.8	34.8	144.9	98.4
GG	41.0	170.3	299.0	59.4	79.3	104.8
NG	61.4	167.1	276.5	48.4	62.5	103.9

the best track after the LPW assimilation. With a continuous forecast time, the reduction in track errors is distinct (refer to Figure 6). By calculation, the 24-, 48-, and 72-hr average forecast track errors are reduced from 57.5, 189.6, and 313.1 km to 47.5, 95.6, and 102.4 km, respectively. The 0- to 72-hr average track error of all nine experiments is 186.7 km in the CTRLs and 81.8 km in the GSI + LPWs. For the LG, the average error is reduced by 59%.

The landfall time also changes before and after LPW assimilation. In the CTRLs, the predicted landfall occurs 7 hr later than the actual landfall. Contrary to CTRLs, LPW assimilations accelerate typhoons in models and make the landfall time consistent with the actual time. Before assimilation, when Hato made landfall at 0450 UTC on 23 August, the bias of the forecasted TC center is greater than 100 km. After LPW assimilation, the landfall error is less than 50 km in three cases and varies between 50 and 100 km in two cases. The simulation using the Thom-NO scheme shows the closest to Hato's actual landing position in the CTRLs. After LPW assimilation, the track error in Thom-NO reduces from 142.0 to 46.8 km.

To identify the sensitivity of the CP or MP scheme selection in TC track prediction, two situations are discussed. In the first situation, one MP scheme remains unchanged and the CP options are modified. In the second situation, the MP schemes are modified, while the CP scheme remains unchanged. In both CTRLs and GSI + LPWs, the average difference among KG, GG, and NG are larger than that among LG, WG, and TG. This demonstrates that the TC track prediction is more sensitive to CP scheme selection before and after LPW assimilation.

In this particular case, the atmospheric circulation field affects the large-scale flow and determines the TC track. To explore this phenomenon, the geopotential heights at 500 hPa for CTRLs and GSI + LPWs are analyzed and compared with reanalysis data from the European Centre for Medium-Range Weather Forecasts (ECMWF). Figure 7 shows a plot of the West Pacific subtropical high (WPSH), which is surrounded by 588 dagpm over the western Pacific, and winds fields from the CTRLs and GSI + LPWs at 1200 UTC on 22 August. Early on 21 August, the WPSH began to strengthen and extend in both northerly and westerly directions. On 22 August, the westernmost part of the WPSH (100–110°E) simulated by GSI + LPWs is further north of that simulated by the CTRLs and closer to the ECMWF analysis. This result causes the simulated TC to migrate in a westward direction.

TC speed is affected by the wind field. The U wind difference before and after assimilation (shaded) is also depicted in Figure 7. In each experiment, the westward flow on the northside of the typhoon and the eastern flow on the southside of the typhoon are strengthened by different degrees after assimilation. This result will cause a faster TC and make landfall consistent with the actual landfall time.

To further illustrate the reasons that the WPSH, as predicted by GSI + LPWs, is farther north than those in the CTRLs, three LPWs from the H-8 observation are compared with the LPW in AF1 (without assimilation) and AF2 (with assimilation; Figure 8). The differences between the three LPWs in AF1 and AF2 are also analyzed. In the lowest layer, the major difference between AF1 and AF2 is located in the Pacific, east of Taiwan. In this area, the PW_low of AF2 is closer to the observations than that of AF1, which indicates that assimilating PW_low adds more water vapor to the TC from the north and east. In the middle layer, two distinct signals exist. The first signal is located similarly to the previous signal, but the difference value is larger. The second signal is located over the South China Sea. Comparisons between AF1 and AF2 with LPW observations indicate that LPW assimilation increases the water content over this area. Additional moist air will favor convective motion and accelerate the TC. The high layer exhibits a difference over the two regions, but the magnitude of the difference is smaller. Of the three layers, LPWs in AF2 are wetter than those in AF1 over the Indochina Peninsula, which contributes to more convection and suppression of downward vertical motion in this region. Thus, the WPSH in AF2 move further west and north than in AF1.
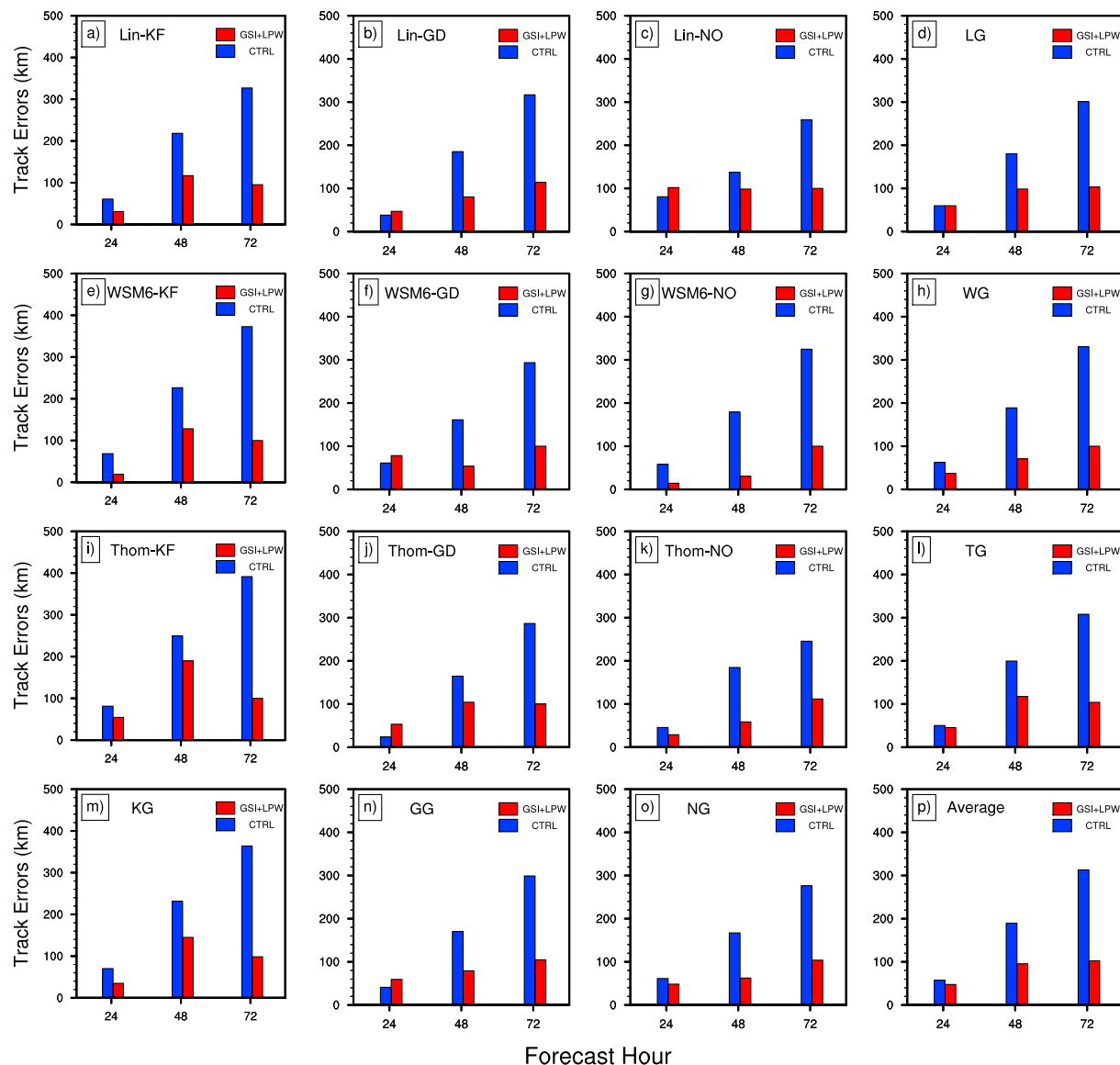
Figure 6. The forecast time series of tropical cyclone Hato track errors in nine experiments: (a) Lin-KF, (b) Lin-GD, (c) Lin-NO, (e) WSM6-KF, (f) WSM6-GD, (g) WSM6-NO, (i) Thom-KF, (j) Thom-GD, and (k) Thom-NO), and group experiments (d) LG, (h) WG, (l) TG, (m) KG, (n) GG, (o) NG), and mean result (p) average for both CTRLs (blue) and Gridpoint Statistical Interpolation + layered precipitable waters (GSI + LPWs; red).

The change in the initial condition after LPW assimilation is also responsible for the fast movement of Hato. An area named SR (Figure 8), where the water vapor is closer to the observations after LPW assimilation, is selected. In the SR region, data assimilation simultaneously changes the initial moisture and temperature information. Due to addition of more water vapor in the middle layers of the SR region after LPW assimilation, more convection tendencies appear in the lower layer. This convection will enhance upward motion in SR and weaken the WPSH. Since the KF scheme allows deep convection with strong updraft as well as downdraft (Kain, 2004), the model convection reaction to LPW assimilation is larger with KF compared with other schemes. The MP process also affects the convection process of SR. Figure 9 shows the time-height cross sections of the SR zonal mean difference (GSI + LPWs minus CTRLs) of hydrometeors versus temperature. Hydrometeors include water vapor, rainwater, cloud water, ice, snow, and graupel, and the phase change between each hydrometeors will affect the temperature. Because more hydrometeors are transported to the upper atmosphere, their condensation or desublimation (evaporation or sublimation) will initially increase (decrease) the atmospheric temperature and release (absorb) latent heat. Above 300 hPa, the
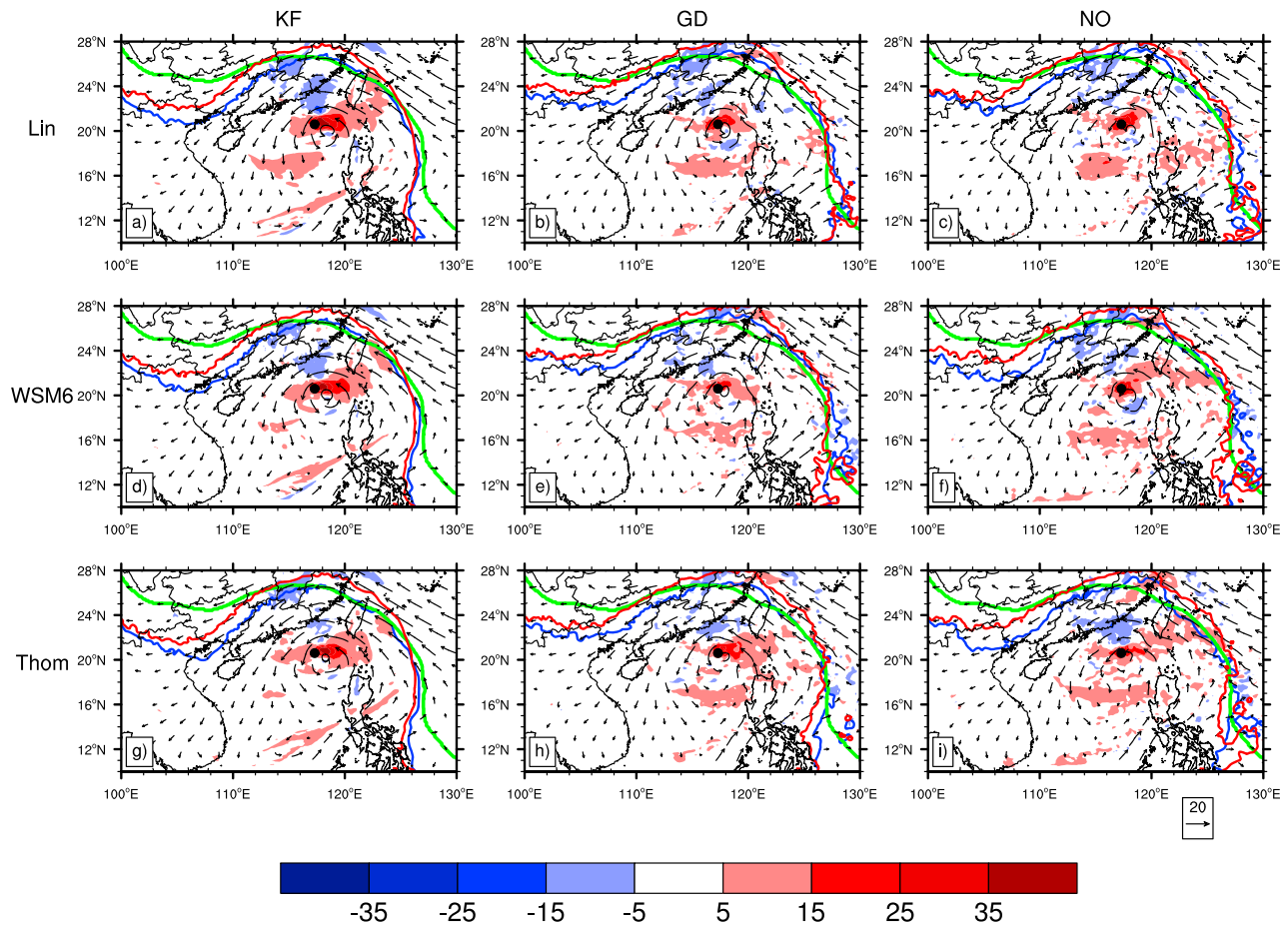
Figure 7. 588 dagpm (unit: 10 m of potential) generate by CTRLs (blue), Gridpoint Statistical Interpolation + layered precipitable waters (GSI + LPWs; red) and European Centre for Medium-Range Weather Forecasts (ECMWF; green), center location of TC Hato from best track data (black dot), wind field from CTRLs (black arrow, unit: m/s), and U wind difference (GSI + LPWs minus CTRLs, unit: m/s) on 500 hPa at 1200 UTC on 22 August with scheme (a) Lin-KF, (b) Lin-GD, (c) Lin-NO, (d) WSM6-KF, (e) WSM6-GD, (f) WSM6-NO, (g) Thom-KF, (h) Thom-GD, and (i)Thom-NO.

atmosphere is warmer due to more solid hydrometeors (ice or snow) condensation and latent heat release. The lower troposphere is simultaneously cooling due to solid hydrometeor sublimation. In different CP and MP combinations, the bias value of the temperature profile differs, but the bias structure remains constant. This different vertical temperature profile in GSI + LPW runs will cause a decrease in the geopotential height at 500 hPa compared with the CTRLs (Sun et al., 2014). This negative bias of geopotential height weakens the resistance of a typhoon in the westward direction and accelerates its movement.

Physically, CP controls the distribution of hydrometeors and MP affects their transformation. Different CPs show different abilities to enhance the convection after adding more water vapor, while different MP schemes strengthen the transformation among different hydrometeor species and further enhance the convection to some extent. Both CP and MP intensify the convection and reduce the WPSH. Figure 9 shows that hydrometeors are redistributed by cumulus convection after LPW assimilation, whereas the difference in hydrometeor species is determined by the MP schemes. The CP process will determine the quantity of hydrometeors involved in the MP process at each level and change the thermal and moisture structure of the large-scale environment. For this reason, CP selection is more critical for TC track prediction.

5.2. Intensity and Thermodynamic Structure

All CTRLs reveal an intensity evolution in terms of the central sea level pressure (CSLP), as shown in Figure 10. In the first 36 hr, CSLP changes show agreement with the observations. As the integral of
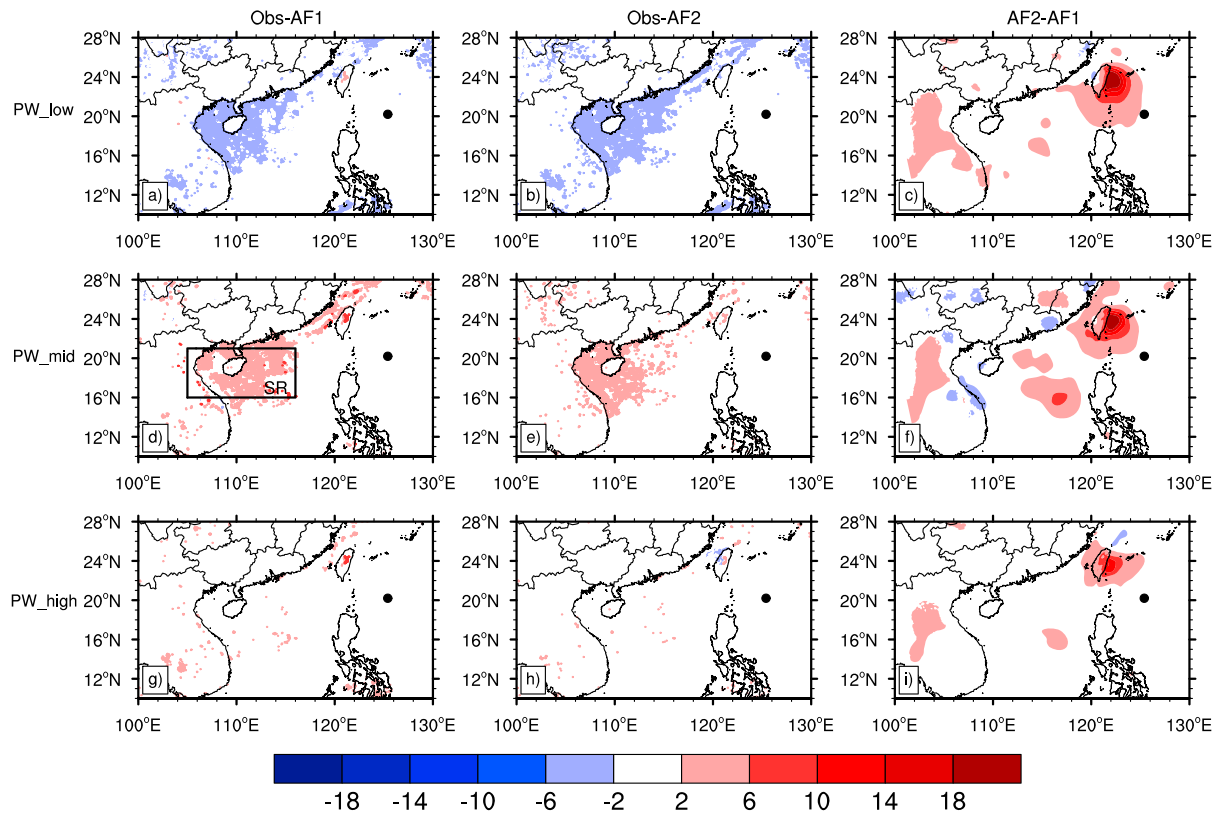
Figure 8. Difference of three layered precipitable waters (LPWs) between observation and AF1 (left panel, observation minus AF1, units: mm, (a) PW_low, (d) PW_mid, and (g) PW_high), observation and AF2 (middle panel, observation minus AF2, units: mm, (b) PW_low, (e) PW_mid, and (h) PW_high), AF2 and AF1 (right panel, AF2 minus AF1, units: mm, (c) PW_low, (f) PW_mid, and (i) PW_high), and center location of TC Hato from best track data (black dot) at 0000 UTC on 21 August 2017.

time increases, the difference becomes evident until landfall is made. The minimum observed CSLP is 965 hPa, whereas the predicted CSLPs fall between 940.7 hPa (WSM6-KF) and 981.6 hPa (Thom-NO). Compared with the CTRLs, the GSI + LPWs are more closely aligned with the observations. In the CTRLs, the simulations using the KF scheme show larger differences than the other schemes; however, after LPW assimilation, the gap between prediction and observation is remarkably diminished. At 1200 UTC on 23 August, the average CSLP error of the KG is 40.2 hPa but decreases to 5.2 hPa after LPW assimilation.

Similar to CSLP, the maximum surface wind (MSW) observed from the best track is 38.6 m/s, whereas the simulated MSW varies between 33.7 m/s (Thom-NO) and 52 m/s (WSM6-KF) in CTRLs and between 32.9 m/s (WSM6-GD) and 47.3 m/s (Lin-KF) in GSI + LPWs. Simulation with the KF scheme has the highest MSW in both CTRLs and GSI + LPWs.

To explore the possible reasons for the intensity difference, the vertical profiles of pseudo-equivalent potential temperature (θ_{se}) are calculated for CTRLs and GSI + LPWs at 1200 UTC on 22 August when the intensity difference begins. Next, the thermodynamic structure during the mature stage of the simulated TC is analyzed. θ_{se} is a comprehensive physical quantity that represents temperature, pressure, and humidity. θ_{se} includes not only the effect of air pressure on temperature but also the effect of water vapor condensation on temperature. The change in θ_{se} with height is a criterion for the instability of convection, which will strengthen or weaken the TC intensity. $\frac{\partial \theta_{se}}{\partial z} < 0$ represents convective instability, $\frac{\partial \theta_{se}}{\partial z} = 0$ represents convective neutrality, and $\frac{\partial \theta_{se}}{\partial z} > 0$ represents convective stability.

At the 36-hr forecast time, all θ_{se} vertical profiles are averaged over a 200-km radius from the typhoon's center, as plotted in Figure 11. In the CTRLs, simulations with the KF scheme have a higher θ_{se} below
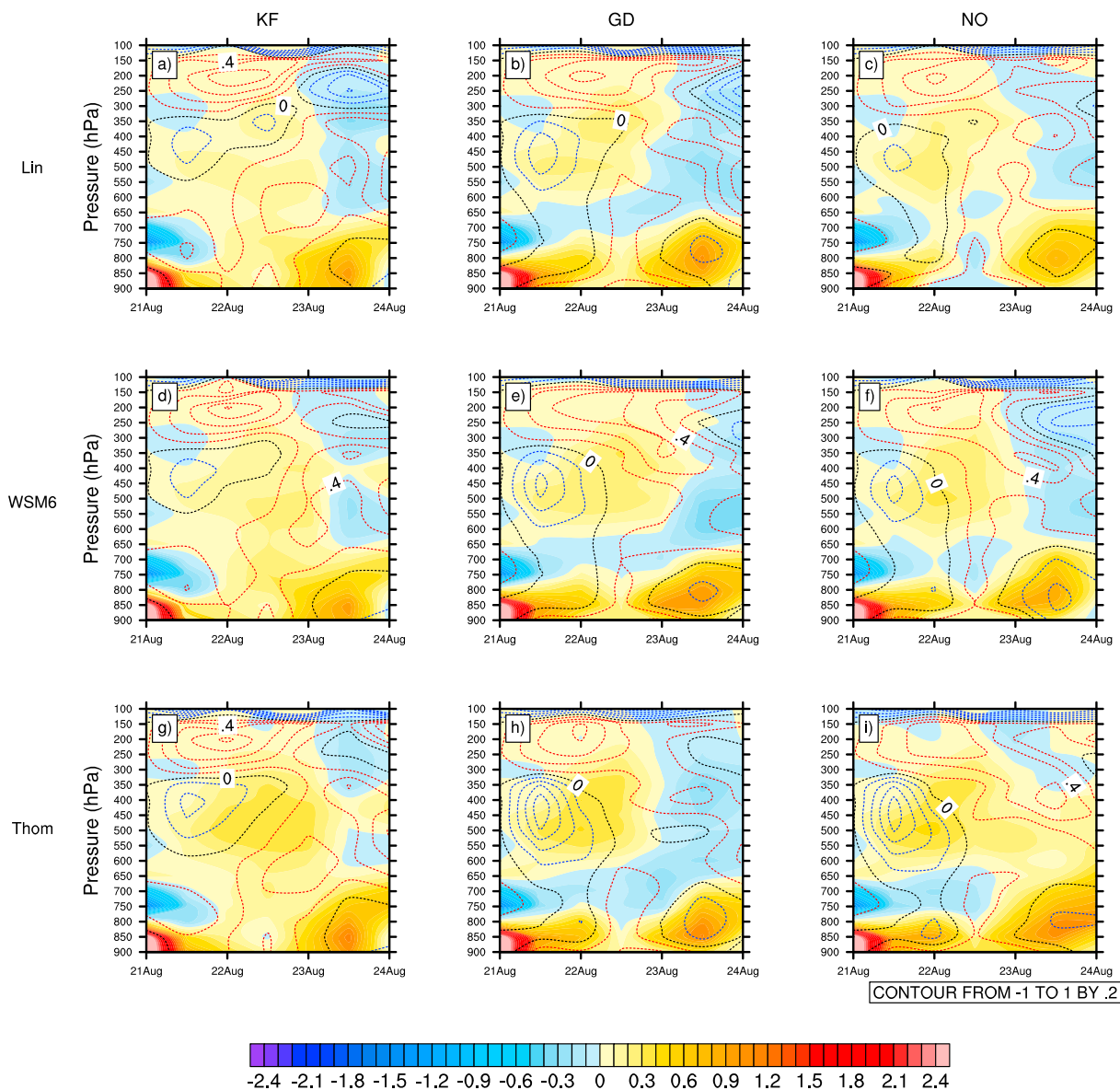
Figure 9. Time-height cross sections of zonal average difference (Gridpoint Statistical Interpolation + layered precipitable waters [GSI + LPWs] minus CTRLs) in hydrometeors (shaded, unit: mm) and temperature (contour, unit: K).

850 hPa, and the height of the convective region is 700 hPa (Lin-KF) and 650 hPa (WSM6-KF and Thom-KF). In this structure, heat will be pumped into the upper air and cause the formation of a typhoon with a significantly warmer core, which strengthens the intensity of the simulated typhoon. After LPW assimilation, the average intensity is strengthened in KG at 1200 UTC on 22 August due to the higher convective region and more convective activity. Conversely, at 1200 UTC on 23 August, the intensity in GSI + LPWs is weaker than in CTRLs since the simulated typhoon Hato persists for approximately 7 hr after landfall in GSI + LPWs. Meanwhile, the simulated typhoon is about to land in the CTRLs. For the GG and NG, most of the predicted intensities in the CTRLs are weaker than the observations with higher CSLP and lower MSW.

The rapid change in typhoon intensity begins at 0000 UTC 22 August and continues to 0000 UTC 23 August when typhoon Hato approaches the area SR. After assimilation of LPWs, more hydrometeors are observed during this period (refer to Figure 9). More water vapor transports from SR to the center of TC through the west wind. Through the CP and MP process, more latent heat is generated due to more water vapor
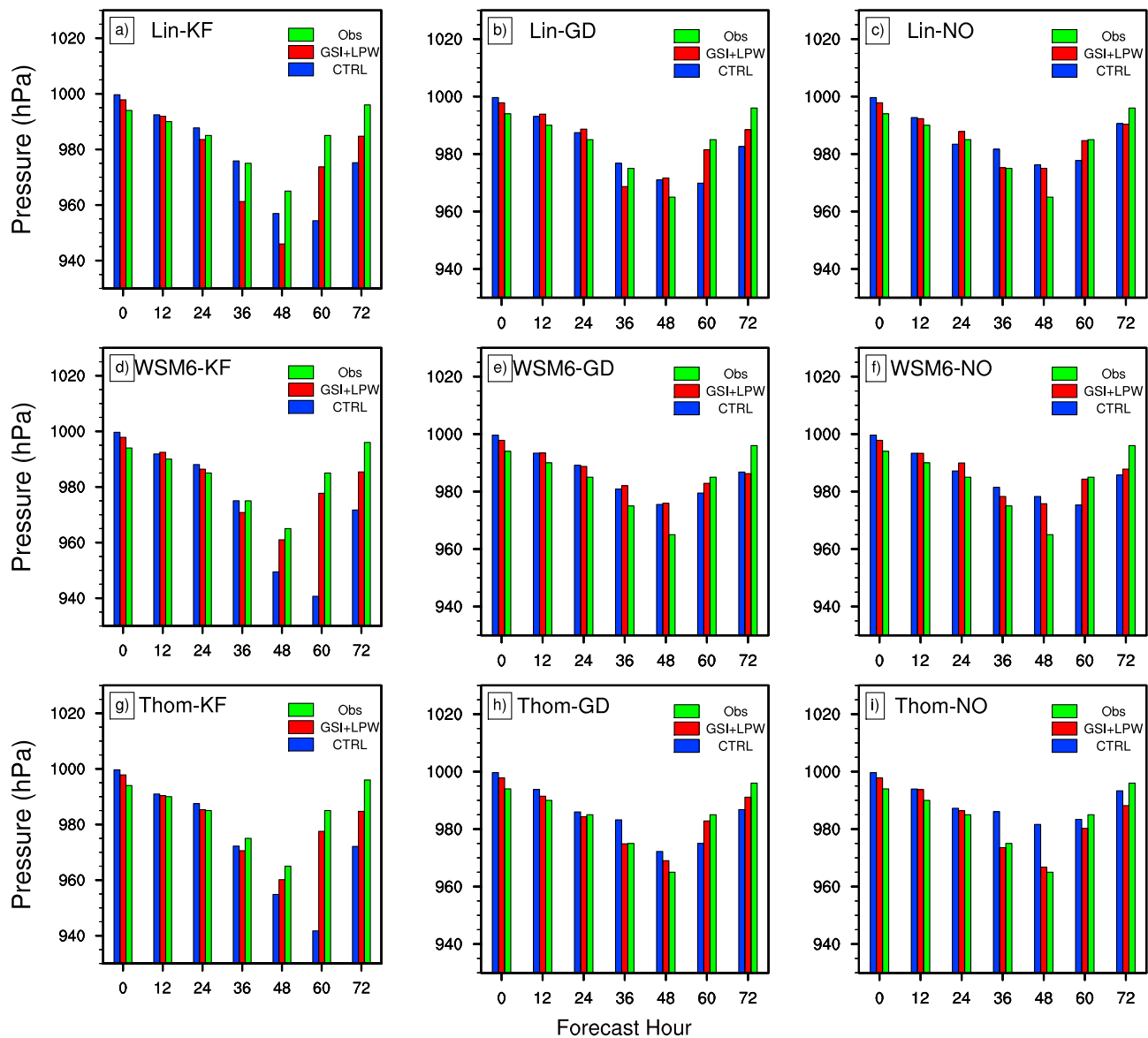
Figure 10. 72-hr forecast of typhoon central pressure (unit: hPa) for CTRLs (blue bar) and Gridpoint Statistical Interpolation + layered precipitable waters (GSI + LPWs; red bar) compared with observation (green bar) from 0000 UTC on 21 to 0000 UTC on 24 August.

participates in the convection activity. Thus, the TC convection is strengthened. The result is a turning point where the height of θ_{se} is rising and the intensity of typhoon is increasing.

To understand the sensitivity of intensity to CP and MP, the following experiment is performed. By keeping the MP scheme constant and comparing θ_{se} profiles with different CP schemes in the CTRLs, the average standard deviations (SDs) of θ_{se} below 500 hPa (the top level of convection) are 1.5 K (LG), 1.0 K (WG), and 0.8 K (TG), respectively. The mean value is 1.1 K compared with 1.0 K when keeping the CP scheme constant. After LPW assimilation, the means of the SDs are reduced to 0.9 K (same MP scheme) and 0.7 K (same CP scheme), respectively. The results conclude that LPW assimilation reduces the differences in the heat release process among the different schemes and weakens the sensitivity of the predicted TC intensity to the MP scheme more than its sensitivity to the CP scheme.

5.3. Precipitation After Landfall

Hato made landfall on 23 August. Figure 12 shows the distribution of the predicted 24-hr cumulative precipitation of this day in the CTRLs, which indicates that the spatial distribution pattern of precipitation is
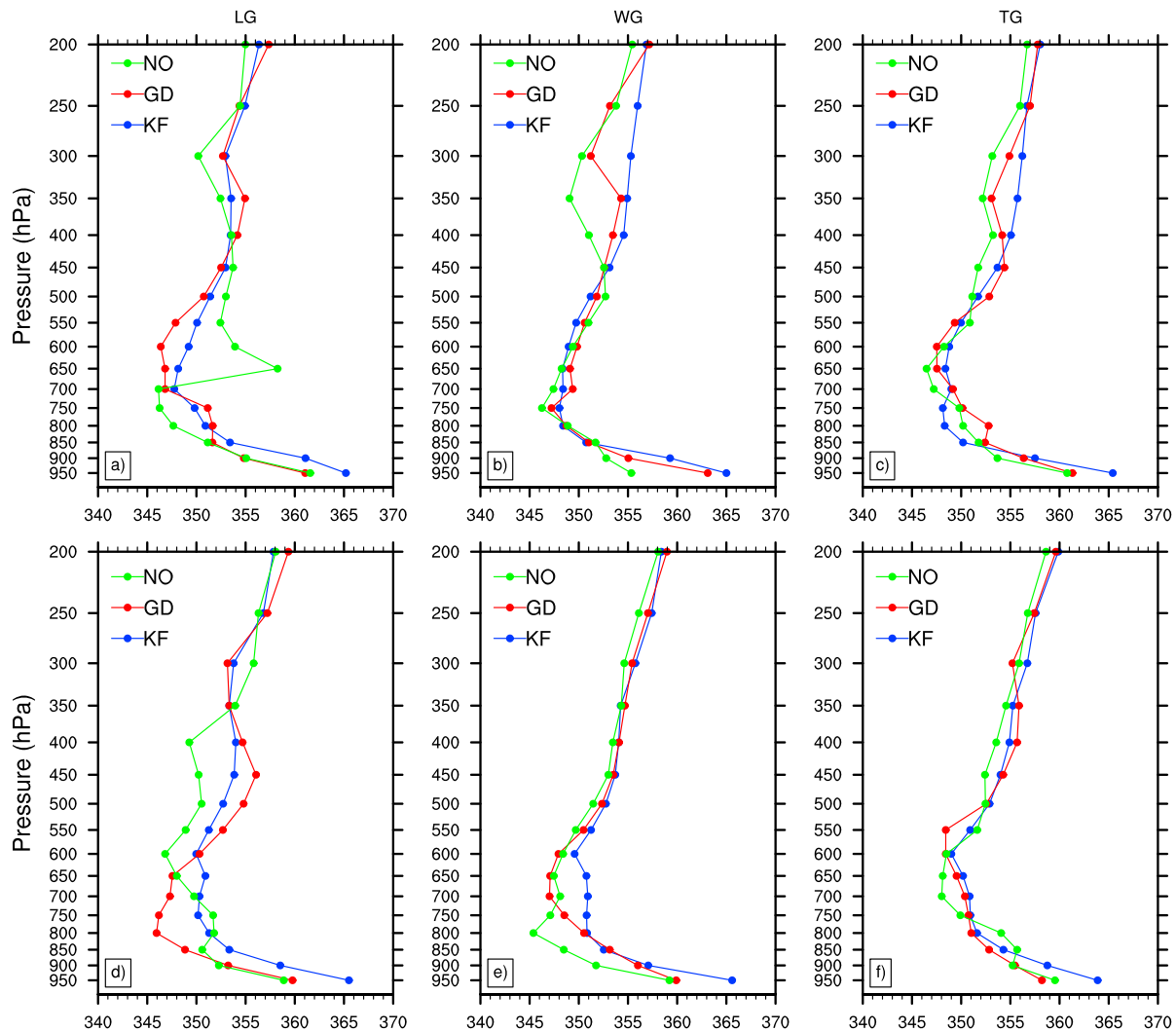
Figure 11. Vertical variation of pseudo equivalent potential temperature average over 200 km from the center for CTRLs (top panel, unit: K, (a) LG, (b) WG, and (c) TG) and Gridpoint Statistical Interpolation + layered precipitable waters (GSI + LPWs; bottom panel, unit: K, (a) LG, (b) WG, and (c) TG) at 36-hr forecast time (1200 UTC on 22 August).

affected by different CP schemes. Using the same CP scheme, the spatial distribution patterns of simulated precipitation with different MP schemes are similar but the rainfall intensity may differ. In the CTRLs, the amount of the predicted precipitation using the KF scheme is less and oriented more to the east than that predicted by other CP schemes. Compared with the observations, GG and NG adequately capture the precipitation spatial pattern. However, the locations of the precipitation centers and the magnitude of rainfall substantially differ. In GG, the maxima of the predicted precipitation occurred in the southern part of the rainstorm area (Lin-GD) or the middle part of the rainstorm area (WSM6-GD and Thom-GD). In NG, the maximum precipitation is located in the west (LIN-NO and Thom-NO) or remains in the middle (WSM6-NO). Of all CTRLs, only the WSM6-NO successfully forecasts strong rainfall in the middle of the Leizhou Peninsula.

To evaluate the quantitative impacts of assimilating LPW data on WRF-predicted heavy rainfall with different combinations of physical options, three skill scores are calculated for each experiment: the equitable threat score (ETS), the probability of detection (POD), and the false alarm ratio (FAR; Ebert et al., 2007; Hamill, 1999). The ETS score shows the fraction of all observed events that were correctly predicted, which is adjusted by random hits (HR) and defined by
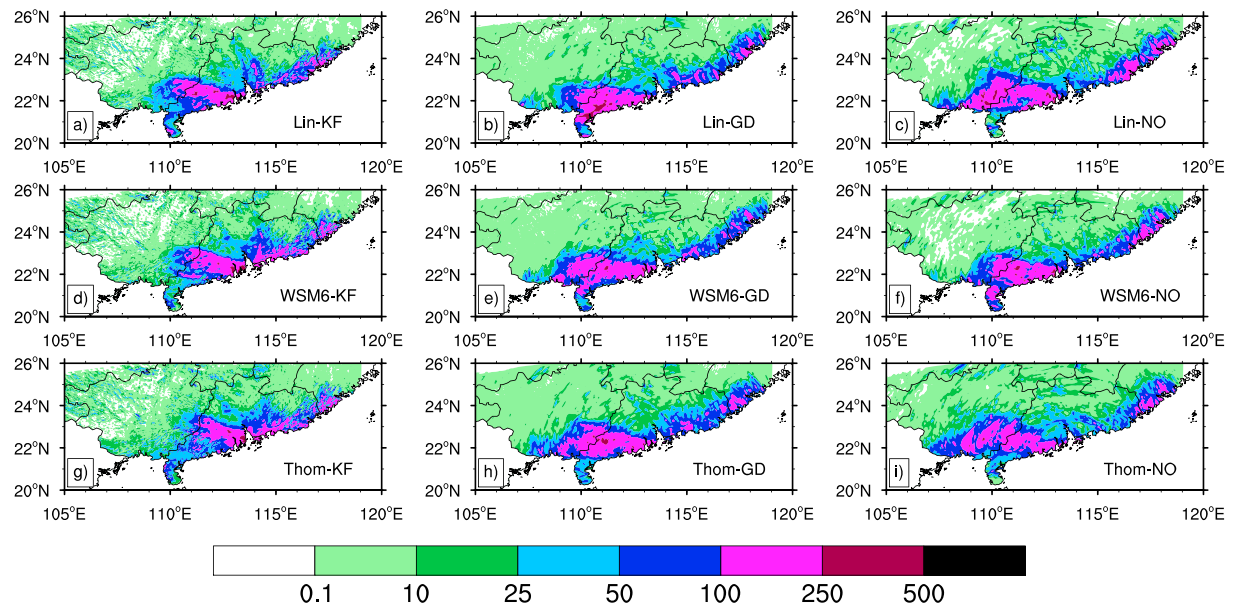
Figure 12. Forecasted 24-hr accumulative precipitation (unit: mm) on August 23 in CTRLs.

$$\text{ETS} = \frac{H - HR}{H + M + FA - HR} \qquad (2)$$

$$HR = \frac{(H + FA)(H + M)}{H + M + FA + CR} \qquad (3)$$

where H, M, FA, and CR represent hits, misses, false alarms, and correct rejection, respectively, as defined in Table 4.

POD represents the fraction of rainfall events that were correctly predicted and defined as follows:

$$\text{POD} = \frac{H}{H + M} \qquad (4)$$

FAR calculates the fraction of predicted rainfall that were false alarms and is represented as

$$\text{FAR} = \frac{FA}{H + FA} \qquad (5)$$

The predicted rainfall in d02, in CTRLs and GSI + LPWs, is compared with the observations. Since Hato made landfall on 23 August, the 24-hr accumulated station rainfall is calculated starting at 0000 UTC and continuing to 2300 UTC of this day to evaluate the heavy rain (>50 mm) prediction skill. The model grid point that is spatially closest to the observation location is selected as the forecast value. Next, the ETS, POD, and FAR are calculated with the results shown in Figure 13. In the CTRLs, the ETS scores are lower in KG than the other schemes for the larger error of the predicted track. Among GG and NG, the difference in the ETS scores using different CP schemes is less than the difference when different MP schemes are employed. Thus, heavy precipitation is more sensitive to the MP schemes of the WRF model.

After LPW assimilation, heavy rainfall prediction improved in the majority of the forecast experiments. The most distinct increase occurs in the

Table 4

Contingency Table Used in Accessing Dichotomous Forecasts and Observations

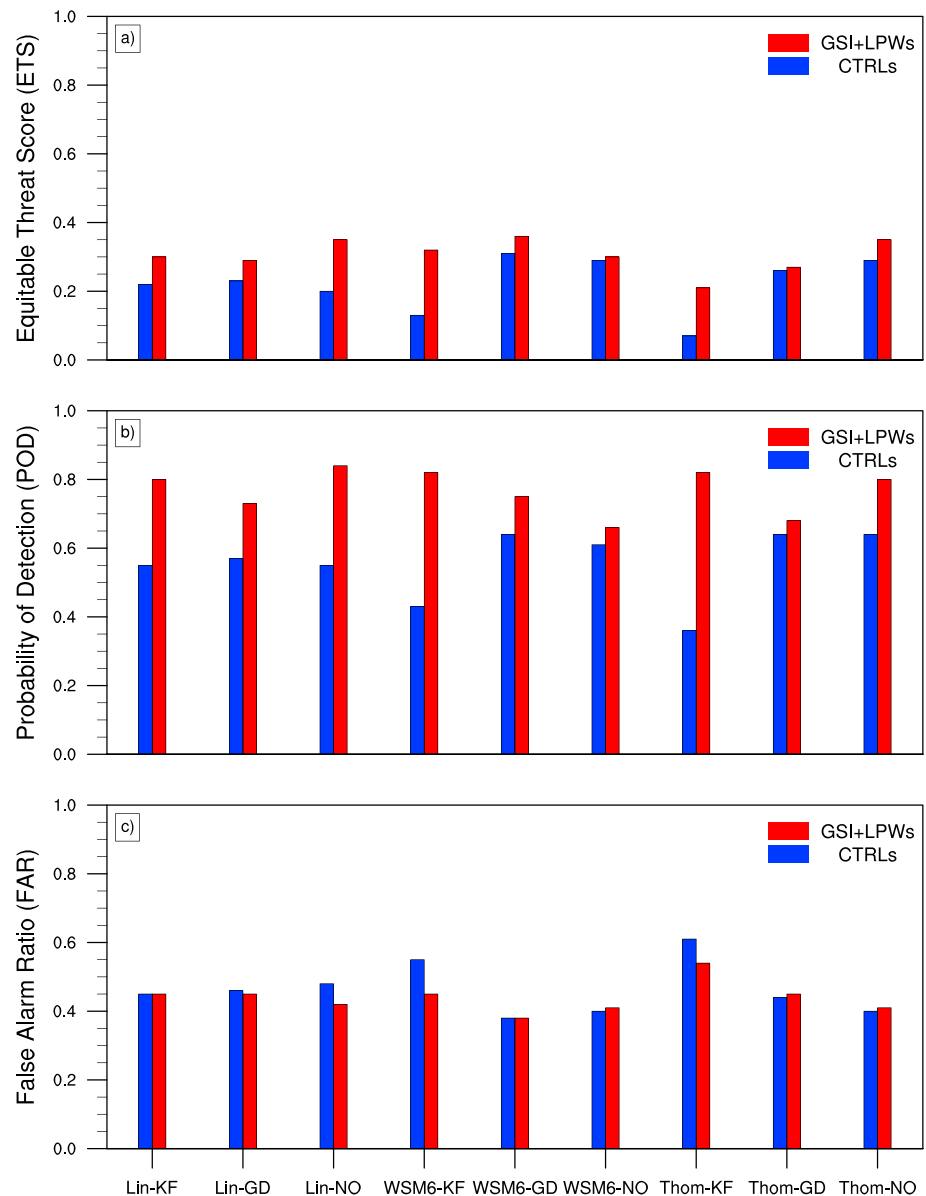|	Observation	
Forecast	Yes	No
Yes	Hits (H)	False alarm
No	Misses (M)	Correct rejection

Figure 13. The (a) equitable threat score (ETS), (b) probability of detection (POD), (c) false alarm ratio (FAR) from CTRLs (blue) and Gridpoint Statistical Interpolation + layered precipitable waters (GSI + LPWs; red) for 24-h rainfall greater than or equal to 50 mm on 23 August.

WSM6-KF, where its ETS increases to 0.32. All PODs show a significant improvement: after LPW assimilation, the WRF can predict the occurrence of more than 50 mm of rainfall at more sites. Note that the POD in the KG increases, which attributes to a more accurate adjustment of the TC track. Contrary to ETS and POD, the LPW assimilation causes three of the FARs to decrease, cause two of the FARs to remain the same, and cause three of the FARs to show slight increases. Even some results show an increase in false alarms, however, their hit numbers show a greater increase; thus, the EST scores continue to increase. Precipitation is associated with track and landfall. After LPW assimilation, the track is closer to reality and the landing time is consistent with the observations, which will change the center location of precipitation and improve the heavy precipitation ETS score.

5.4. Comparison of Forecast From Different Initial Times

Three additional initial times—0000 UTC and 1200 UTC on 20 and 1200 UTC on 21 August (near the formation time of TC Hato)—are selected to initialize the experiments. The model physical settings are the same as
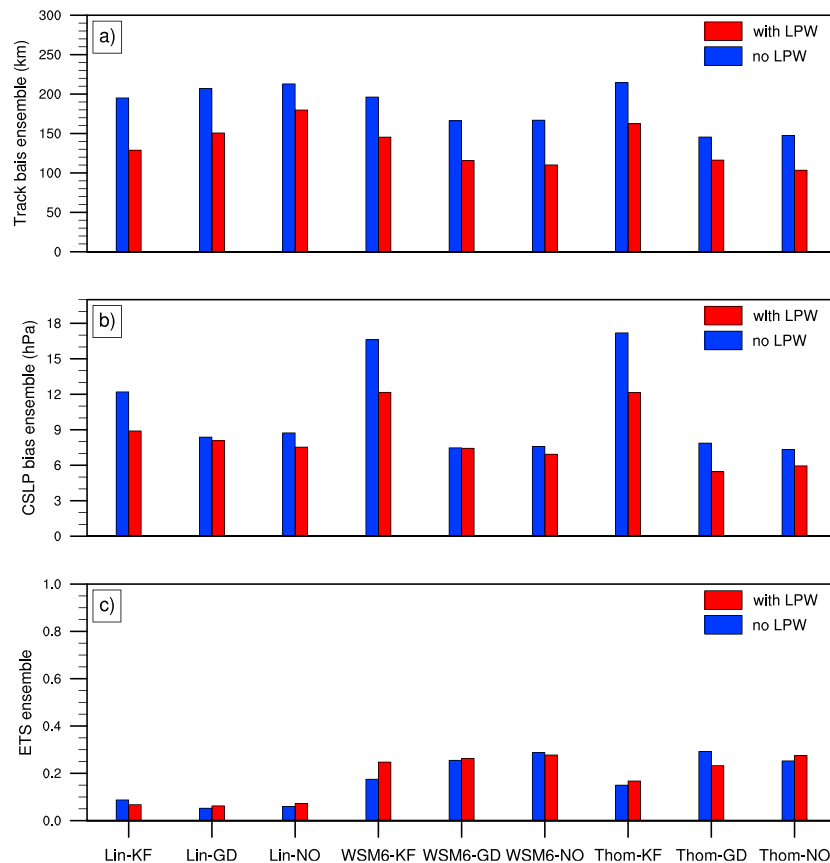
Figure 14. Average of (a) track bias, (b) central sea level pressure (CSLP) bias, and (c) equitable threat score (ETS) with same forecasting time but different initial time in all nine combinations.

the CTRL physical settings, and the assimilation settings are the same as the GSI + LPW assimilation settings, with the exception that the assimilated LPW data are collected at different initial times. Because the lifetime of Hato is short, the longest forecast time is 120 hr and starts at 0000 UTC on 20 August; however, only 96-hr results are selected for analysis. The results with different initial times but the same forecasting time—0000 UTC 22, 0000 UTC 23, and 0000 UTC 24—are selected. For one experiment with a specific CP and MP combination, 12 outputs (four initial times and three forecast times) comprise a group. The average bias of the track and CSLP in each group is computed. The ETS group statistic mean (four initial time) of 24-hr heavy rain forecast from 0000 UTC to 2300 UTC on 23 August are calculated. The group statistic mean results for the nine group experiments are shown in Figure 14.

The track bias with LPW decreases in all cases, and the average bias value is 48.8 km. The landfall time lags are reduced in all experiments even if some time lag still exists (the forecast landing time and the real landing time) in the experiments with LPW assimilation at an earlier initial time. The comparison of results with different CP and MP combinations revealed that the cases with the KF scheme show the most improvement in the track forecast. The CSLP bias also shows a decrease after LPW assimilation in all experiments. The average value is reduced from 10.3 to 8.2 hPa. The forecasts using the KF scheme also show the maximum decrease. The ETS group statistic mean does not exhibit a distinct improvement after LPW assimilation. One reason is that the landing time and location are not consistent with reality even though LPW assimilation minimized the track bias. Especially in forecasts with earlier initial times, this bias generates almost no prediction skill in heavy rain after landfall; however, a slight improvement occurs after LPW assimilation. The maximum increase in ETS of all experiments is 0.07, and the average improvement value of the nine groups is only 0.01.

In general, the group statistic results indicate that the LPW shows a positive effect on the predictions of Hato's track, intensity, and heavy rain with different initial times.

6. Summaries

A series of nine sensitivity experiments using various combinations of CP and MP schemes were conducted with the WRF model to predict Typhoon Hato, which is one of the strongest typhoons to make landfall in the South China Sea region. LPW data retrieved from H-8 are assimilated into the WRF using a GSI assimilation system to test the impact on TC track, intensity, and precipitation with different schemes. Possible reasons for the various results are also explored in this paper. Our findings are described as follows:

1. In general, all CTRLs show the westward movement of the TC but fail to accurately predict the time of landfall. Due to reduction in track error after LPW assimilation, the predicted landing time shows consistent with the observation. The reason is that H-8 increases the amount of water vapor in atmosphere, and causing the WPSH becomes weaker and closer to reality through CP and MP process. TC speed is also accelerated by this large-scale environment change. Based on sensitivity study, the results reveal that the CP schemes enable better control of the typhoon track than the MP schemes both before and after LPW assimilation.

2. The TC forecast intensity is analyzed in terms of CSLP and MSW. In the first 36 hr, the results in both CTRLs and GSI + LPWs concur with the observations but show a significant difference afterward. The deviations are caused by not only differences in the forecast track but also the profiles of θ_{se}, which affect the typhoon's thermodynamic structure and determine the intensity. The sensitivity analysis shows that intensity prediction relies on the CP and MP schemes. LPW assimilation weakens the sensitivity of the predicted intensity to MP schemes more than to CP schemes.

3. CP schemes have a distinct impact on the precipitation patterns, whereas MP schemes affect rain intensity. LPW assimilation directly adjusts the water vapor content in the atmosphere and helps to improve the accuracy of predicting heavy rainstorms. The calculations in this study indicate that the ETS and the POD of heavy rain (>50 mm) are increased after assimilation. Conversely, some FAR results indicate only slight increases after LPW assimilation, while their POD increase more and will not decrease the ETS.

4. The group statistical results with different initial times, but the same forecast time also indicates the positive impact of LPW on Hato prediction. Assimilation of LPW with the KF scheme shows the most improvement.

Two additional group experiments are conducted. One group assimilates only satellite radiance (RAD), whereas the other group assimilates both satellite radiance and LPWs (RAD + LPW). The satellite radiance data sets are obtained from UCAR: the Advanced Microwave Sounding Unit-A (AMSU-A), the High resolution Infrared Radiation Sounder (HIRS-4), the Microwave Humidity Sounder (MHS), the Atmospheric Infrared Sounder (AIRS), the Advanced Tech Microwave Sounder (ATMS), and the Infrared Atmospheric Sounding interferometer (IASI from MetOp-2; http://rda.ucar.edu/datasets/ds735.0/). The same assimilation system is employed in this study (GSI version 3.3). The RAD assimilation is adopted in d01 with an NAM background error covariance matrix. The time window is ±0.5 hr, and the thinning box contains 60 km (for AMSU-A, AIRS) and 120 km (for HIRS-4, MHS, ATMS, and IASI). The WRF settings are the same for the GSI + LPWs. The results show that assimilating satellite radiance data has a negative effect on the forecast results comparing with the output of CTRLs. In this case, adding LPW data can improve the forecast results for both GSI + LPWs and RAD + LPWs. The side effect of satellite radiance in RAD + LPWs may be attributed to the quality control of satellite data. Therefore, techniques for combining satellite radiance and LPWs in TC forecast will be a topic for future research.

In this paper, we examine the impact of LPW assimilation on TC prediction for Typhoon Hato. Although the paper focuses on the TC ambient atmosphere, the response of CP and MP to data assimilation in TC requires more observation data (in or around TC) for future analysis. The parameterization function is influenced by many factors, including case and model resolution. Hato is the strongest typhoon that is available for a case study because operational H-8 data are available only after July 2015. Additional H-8 observational data are needed to analyze the sensitivity of LPW assimilation on different parameters, such as planetary boundary layer schemes, in future research. With hyperspectral IR sounders such as GIIRS (Yang et al., 2017) onboard the geostationary orbit, more vertical moisture information with high temporal resolution (Schmit et al., 2009) can be applied to achieve further improvements in TC and local severe storm prediction (Li et al., 2018).

References

Anthes, R. A. (1982). *Tropical cyclones: Their evolution, structure and effects*. Boston, MA: American Meteorological Society. https://doi.org/10.1007/978-1-935704-28-7

Arakawa, A. (2004). The cumulus parameterization problem: Past, present, and future. *Journal of Climate*, *17*(13), 2493–2525. https://doi.org/10.1175/1520-0442(2004)017<2493:RATCPP>2.0.CO;2

Baldauf, M., & Brdar, S. (2013). An analytic solution for linear gravity waves in a channel as a test for numerical models using the non-hydrostatic, compressible Euler equations. *Quarterly Journal of the Royal Meteorological Society*, *139*(677), 1977–1989. https://doi.org/10.1002/qj.2105

Bauer, P., Geer, A. J., Lopez, P., & Salmond, D. (2010). Direct 4D-Var assimilation of all-sky radiances. Part I: Implementation. *Quarterly Journal of the Royal Meteorological Society*, *136*(652), 1868–1885. https://doi.org/10.1002/qj.659

Bauer, P., Thorpe, A., & Brunet, G. (2015). The quiet revolution of numerical weather prediction. *Nature*, *525*(7567), 47–55. https://doi.org/10.1038/nature14956

Bessho, K., Date, K., Hayashi, M., Ikeda, A., Imai, T., Inoue, H., et al. (2016). An introduction to Himawari-8/9—Japan's New-Generation Geostationary Meteorological Satellites. *Journal of the Meteorological Society of Japan. Ser. II*, *94*(2), 151–183. https://doi.org/10.2151/jmsj.2016-009

Biswas, M. K., Bernardet, L., & Dudhia, J. (2014). Sensitivity of hurricane forecasts to cumulus parameterizations in the HWRF model. *Geophysical Research Letters*, *41*, 9113–9119. https://doi.org/10.1002/2014GL062071

Cardinali, C. (2009). Monitoring the observation impact on the short-range forecast. *Quarterly Journal of the Royal Meteorological Society*, *135*(638), 239–250. https://doi.org/10.1002/qj.366

Chen, F., & Dudhia, J. (2001). Coupling an advanced land surface hydrology model with the Penn state NCAR MM5 modeling system. Part I: Model implementation and sensitivity. *Monthly Weather Review*, *129*(4), 569–585. https://doi.org/10.1175/1520-0493(2001)129<0569:CAALSH>2.0.CO;2

de Rooy, W. C., Bechtold, P., Frohlich, K., Hohenegger, C., Jonker, H., Mironov, D., et al. (2013). Entrainment and detrainment in cumulus convection: An overview. *Quarterly Journal of the Royal Meteorological Society*, *139*(670), 1–19. https://doi.org/10.1002/qj.1959

Dudhia, J. (1989). Numerical study of convection observed during the winter monsoon experiment using a mesoscale two-dimensional model. *Journal of Atmospheric Science*, *46*(20), 3077–3107. https://doi.org/10.1175/1520-0469(1989)046<3077:NSOCOD>2.0.CO;2

Duruisseau, F., Chambon, P., Guedj, S., Guidard, V., Fourrie, N., Taillefer, F., et al. (2017). Investigating the potential benefit to a mesoscale NWP model of a microwave sounder on board a geostationary satellite. *Quarterly Journal of the Royal Meteorological Society*, *143*(706), 2104–2115. https://doi.org/10.1002/qj.3070

Ebert, E. E., Janowiak, J. E., & Kidd, C. (2007). Comparison of near-real-time precipitation estimates from satellite observations and numerical models. *Bulletin of the American Meteorological Society*, *88*(1), 47–64. https://doi.org/10.1175/BAMS-88-1-47. https://doi.org/10.1175/BAMS-88-1-47

Efstathiou, G. A., Zoumakis, N. M., Melas, D., Lolis, C. J., & Kassomenos, P. (2013). Sensitivity of WRF to boundary layer parameterizations in simulating a heavy rainfall event using different microphysical schemes. Effect on large-scale processes. *Atmospheric Research*, *132-133*(10), 125–143. https://doi.org/10.1016/j.atmosres.2013.05.004

Fowler, L. D., & Randall, D. A. (2002). Interactions between cloud microphysics and cumulus convection in a general circulation model. *Journal of Atmospheric Science*, *59*(21), 3074–3098. https://doi.org/10.1175/1520-0469(2002)059<3074:IBCMAC>2.0.CO;2

Franklin, C. N., Holland, G. J., & May, P. T. (2005). Sensitivity of tropical cyclone rainbands to ice-phase microphysics. *Monthly Weather Review*, *133*(8), 2473–2493. https://doi.org/10.1175/MWR2989.1

Geer, A. J., Lonitz, K., Weston, P., Kazumori, M., Okamoto, K., Zhu, Y., et al. (2018). All-sky satellite data assimilation at operational weather forecasting centres. *Quarterly Journal of the Royal Meteorological Society*, *144*(713), 1191–1217. https://doi.org/10.1002/qj.3202

Grell, G. A., & Dévényi, D. (2002). A generalized approach to parameterizing convection combining ensemble and data assimilation techniques. *Geophysical Research Letters*, *29*(6), D06301. https://doi.org/10.1029/2002GL015311

Gross, M., Wan, H., Rasch, P. J., Caldwell, P. M., Williamson, D. L., Klocke, D., et al. (2018). Physics-dynamics coupling in weather, climate, and Earth system models: Challenges and recent progress. *Monthly Weather Review*, *146*(11), 3505–3544. https://doi.org/10.1175/MWR-D-17-0345.1

Gustafson, W. I. Jr., Ma, P.-L., Xiao, H., Singh, B., Rasch, P. J., & Fast, J. D. (2013). The Separate Physics and Dynamics Experiment (SPADE) framework for determining resolution awareness: A case study of microphysics. *Journal of Geophysical Research: Atmospheres*, *118*, 9258–9276. https://doi.org/10.1002/jgrd.50711

Hamill, T. M. (1999). Hypothesis tests for evaluating numerical precipitation forecasts. *Weather and Forecasting*, *14*(2), 155–167. https://doi.org/10.1175/1520-0434(1999)014<0155:HTFENP>2.0.CO;2

Hong, S.-Y., & Lim, J.-O. J. (2006). The WRF single-moment 6-class microphysics scheme (WSM6). *Journal of the Korean Meteorological Society*, *42*(2), 129–151.

Hong, S.-Y., Noh, Y., & Dudhia, J. (2006). A new vertical diffusion package with an explicit treatment of entrainment processes. *Monthly Weather Review*, *134*(9), 2318–2341. https://doi.org/10.1175/MWR3199.1

Jankov, I., Gallus, W. A. Jr., Segal, M., & Koch, S. E. (2007). Influence of initial conditions on the WRF-ARW model QPF response to physical parameterization changes. *Weather and Forecasting*, *22*(3), 501–519. https://doi.org/10.1175/WAF998.1

Jin, X., Li, J., Schmit, T. J., Li, J., Goldberg, M. D., & Gurka, J. J. (2008). Retrieving clear-sky atmospheric parameters from SEVIRI and ABI infrared radiances. *Journal of Geophysical Research*, *113*, D15310. https://doi.org/10.1029/2008JD010040

Kain, J. S. (2004). The Kain-Fritsch convective parameterization: An update. *Journal of Applied Meteorology*, *43*(1), 170–181. https://doi.org/10.1175/1520-0450(2004)043<0170:TKCPAU>2.0.CO;2

Kanase, R. D., & Salvekar, P. S. (2015). Effect of physical parameterization schemes on track and intensity of cyclone LAILA using WRF model. *Asia-Pacific Journal of Atmospheric Sciences*, *51*(3), 205–227. https://doi.org/10.1007/s13143-015-0071-8

Kleist, D. T., Parrish, D. F., Derber, J. C., Treadon, R., Wu, W. S., & Lord, S. (2009). Introduction of the GSI into the NCEP global data assimilation system. *Weather and Forecasting*, *24*(6), 1691–1705. http://doi.org/10.1175/2009WAF2222201.1

Kuang, Z. (2010). Linear Response Functions of a Cumulus Ensemble to Temperature and Moisture Perturbations and Implications for the Dynamics of Convectively Coupled Waves. *Journal of the Atmospheric Sciences*, *67*(4), 941–962. https://doi.org/10.1175/2009JAS3260.1

Lee, Y.-K., Li, J., Li, Z., & Schmit, T. (2017). Atmospheric temporal variations in the pre-landfall environment of Typhoon Nangka (2015) observed by the Himawari-8 AHI. *Asia-Pacific Journal of Atmospheric Sciences*, *53*(4), 431–443. https://doi.org/10.1007/s13143-017-0046-z

Lee, Y. K., Li, Z., Li, J., & Schmit, T. J. (2014). Evaluation of the GOES-R ABI LAP Retrieval Algorithm Using theGOES-13Sounder. *Journal of Atmospheric and Oceanic Technology*, *31*(1), 3–19. https://doi.org/10.1175/JTECH-D-13-00028.1

Li, J., Li, J., Otkin, J., Schmit, T. J., & Liu, C. Y. (2011). Warning information in a preconvection environment from the geostationary advanced infrared sounding system-a simulation study using the IHOP case. *Journal of Applied Meteorology and Climatology*, *50*(3), 776–783. https://doi.org/10.1175/2010JAMC2441.1

Li, J., Liu, C. Y., Zhang, P., & Schmit, T. J. (2012). Applications of full spatial resolution space-based advanced infrared soundings in the preconvection environment. *Weather and Forecasting*, *27*(2), 515–524. https://doi.org/10.1175/WAF-D-10-05057.1

Li, J., & Liu, H. (2009). Improved hurricane track and intensity forecast using single field-of-view advanced IR sounding measurements. *Geophysical Research Letters*, *36*, L11813. https://doi.org/10.1029/2009GL038285

Li, J., Wang, P., Han, H., Li, J., & Zheng, J. (2016). On the assimilation of satellite sounder data in cloudy skies in numerical weather prediction models. *Journal of Meteorological Research*, *30*(2), 169–182. https://doi.org/10.1007/s13351-016-5114-2

Li, J., Wolf, W. W., Menzel, W. P., Zhang, W., Huang, H.-L., & Achtor, T. H. (2000). Global soundings of the atmosphere from ATOVS measurements: The algorithm and validation. *Journal of Applied Meteorology*, *39*(8), 1248–1268. https://doi.org/10.1175/1520-0450 (2000)039<1248:GSOTAF>2.0.CO;2

Li, X. (2013). Sensitivity of WRF simulated typhoon track and intensity over the Northwest Pacific Ocean to cumulus schemes. *Science China Earth Sciences*, *56*(2), 270–281. https://doi.org/10.1007/s11430-012-4486-0

Li, X., & Pu, Z. (2008). Sensitivity of numerical simulation of early rapid intensification of Hurricane Emily (2005) to cloud microphysical and planetary boundary layer parameterizations. *Monthly Weather Review*, *136*(12), 4819–4838. https://doi.org/10.1175/2008MWR 2366.1

Li, Z., Li, J., Wang, P., Lim, A., Li, J., Schmit, T. J., et al. (2018). Value-added Impact of Geostationary Hyperspectral Infrared Sounders on Local Severe Storm Forecasts—via a Quick Regional OSSE. *Advances in Atmospheric Sciences*, *35*(10), 1217–1230. https://doi.org/ 10.1007/s00376-018-8036-3

Lin, K. J., Yang, S. C., & Chen, S. S. (2018). Reducing TC position uncertainty in an ensemble data assimilation and prediction system: A case study of typhoon Fanapi (2010). *Weather and Forecasting*, *33*(2), 561–582. https://doi.org/10.1175/WAF-D-17-0152.1

Lin, Y. L., Farley, R. D., & Orville, H. D. (1983). Bulk parameterization of the snow field in a cloud model. *Journal of Applied Meteorology*, *22*(6), 1065–1092. https://doi.org/10.1175/1520-0450(1983)022<1065:BPOTSF>2.0.CO;2

Liu, H., & Li, J. (2010). An improvement in forecasting rapid intensification of typhoon sinlaku (2008) using clear-sky full spatial resolution advanced IR soundings. *Journal of Applied Meteorology and Climatology*, *49*(4), 821–827. https://doi.org/10.1175/2009JAMC2374.1

Ma, Z., Maddy, E. S., Zhang, B., Zhu, T., & Boukabara, S. A. (2017). Impact Assessment of Himawari-8AHI Data Assimilation in NCEP GDAS/GFS with GSI. *Journal of Atmospheric and Oceanic Technology*, *34*(4), 797–815. https://doi.org/10.1175/JTECH-D-16-0136.1

le Marshall, J., Jung, J., Derber, J., Chahine, M., Treadon, R., Lord, S. J., et al. (2006). Improving global analysis and forecasting with airs. *Bulletin of the American Meteorological Society*, *87*(7), 891–895. https://doi.org/10.1175/BAMS-87-7-891

Mendelsohn, R., Emanuel, K., Chonabayashi, S., & Bakkensen, L. (2012). The impact of climate change on global tropical cyclone damage. *Nature Climate Change.*, *2*(3), 205–209. https://doi.org/10.1038/nclimate1357

Migliorini, S. (2012). On the equivalence between radiance and retrieval assimilation. *Monthly Weather Review*, *140*(1), 258–265. https:// doi.org/10.1175/MWR-D-10-05047.1

Mlawer, E. J., Taubman, S. J., Brown, P. D., Iacono, M. J., & Clough, S. A. (1997). Radiative transfer for inhomogeneous atmospheres: RRTM, a validated correlated-k model for the longwave. *Journal of Geophysical Research*, *102*(D14), 16,663–16,682. https://doi.org/ 10.1029/97JD00237

Mohan, P., & Strobl, E. (2017). The short-term economic impact of tropical cyclone pam: An analysis using VIIRS nightlight satellite imagery. *International Journal of Remote Sensing*, *38*(21), 5992–6006. https://doi.org/10.1080/01431161.2017.1323288

Nasrollahi, N., Aghakouchak, A., Li, J., Gao, X., Hsu, K., & Sorooshian, S. (2012). Assessing the impacts of different WRF precipitation physics in hurricane simulations. *Weather and Forecasting*, *27*(4), 1003–1016. https://doi.org/10.1175/WAF-D-10-05000.1

Nie, J., & Kuang, Z. (2012). Responses of shallow cumulus convection to large-scale temperature and moisture perturbations: A comparison of large-eddy simulations and a convective parameterization based on stochastically entraining parcels. *Journal of the Atmospheric Sciences*, *69*(6), 1936–1956. https://doi.org/10.1175/JAS-D-11-0279.1

Parrish, D. F., & Derber, J. C. (1992). The National Meteorological Center's spectral statistical-interpolation analysis system. *Monthly Weather Review*, *120*(8), 1747–1763. https://doi.org/10.1175/1520-0493(1992)120<1747:TNMCSS>2.0.CO;2

Pu, Z., & Zhang, L. (2010). Validation of Atmospheric Infrared Sounder temperature and moisture profiles over tropical oceans and their impact on numerical simulations of tropical cyclones. *Journal of Geophysical Research*, *115*, D24114. https://doi.org/10.1029/ 2010JD014258

Raju, P. V. S., Potty, J., & Mohanty, U. C. (2011). Sensitivity of physical parameterizations on prediction of tropical cyclone Nargis over the bay of Bengal using WRF model. *Meteorology and Atmospheric Physics*, *113*(3–4), 125–137. https://doi.org/10.1007/s00703-011-0151-y

Rakesh, V., Singh, R., Pal, P. K., & Joshi, P. C. (2009). Impacts of satellite-observed winds and total precipitable water on WRF short-range forecasts over the Indian region during the 2006 summer monsoon. *Weather and Forecasting*, *24*(6), 1706–1731. https://doi.org/10.1175/ 2009WAF2222242.1

Reisner, J., Rasmussen, R. M., & Bruintjes, R. T. (1998). Explicit forecasting of supercooled liquid water in winter storms using the MM5 mesoscale model. *Quarterly Journal of the Royal Meteorological Society*, *124*(548), 1071–1107. https://doi.org/10.1002/qj.49712454804

Schmit, T. J., Griffith, P., Gunshor, M. M., Daniels, J. M., Goodman, S. J., & Lebair, W. J. (2017). A closer look at the ABI on the GOES-R series. *Bulletin of the American Meteorological Society*, *98*(4), 681–698. https://doi.org/10.1175/BAMS-D-15-00230.1

Schmit, T. J., Gunshor, M. M., Menzel, W. P., Gurka, J. J., Li, J., & Bachmeier, A. S. (2005). Introducing the next-generation advanced baseline imager on GOES-R. *Bulletin of the American Meteorological Society*, *86*(8), 1079–1096. https://doi.org/10.1175/BAMS-86-8-1079

Schmit, T. J., Li, J., Ackerman, S. A., & Gurka, J. J. (2009). High-Spectral- and High-Temporal-Resolution Infrared Measurements from Geostationary Orbit. *Journal of Atmospheric and Oceanic Technology*, *26*(11), 2273–2292. https://doi.org/10.1175/2009JTECHA1248.1

Schmit, T. J., Li, J., Li, J., Feltz, W., Gurka, J. J., Goldberg, M. D., & Schrab, K. (2008). The GOES-R advanced baseline imager and the continuation of current sounder products. *Journal of Applied Meteorology and Climatology*, *47*(10), 2696–2711. https://doi.org/10.1175/ 2008JAMC1858.1

Seemann, S. W., Borbas, E. E., Knuteson, R. O., Stephenson, G. R., & Huang, H.-L. (2008). Development of a global infrared land surface emissivity database for application to clear sky sounding retrievals from multispectral satellite radiance measurements. *Journal of Applied Meteorology and Climatology*, *47*(1), 108–123. https://doi.org/10.1175/2007JAMC1590.1

Shao, H., Derber, J., Huang, X.-Y., Hu, M., Newman, K., Stark, D., et al. (2016). Bridging research to operations transitions status and plans of community GSI. *Bulletin of the American Meteorological Society*, *97*(8), 1427–1440. https://doi.org/10.1175/BAMS-D-13-00245.1

Song, X., & Zhang, G. J. (2011). Microphysics parameterization for convective clouds in a global climate model: Description and single-column model tests. *Journal of Geophysical Research*, *116*, D02201. https://doi.org/10.1029/2010JD014833

Srinivas, C. V., Bhaskar Rao, D. V., Yesubabu, V., Baskaran, R., & Venkatraman, B. (2012). Tropical cyclone predictions over the bay of Bengal using the high-resolution advanced research Weather Research and Forecasting (ARW) model. *Quarterly Journal of the Royal Meteorological Society*, *139*(676), 1810–1825. https://doi.org/10.1002/qj.2064

Stensrud, D. J. (2007). *Parameterization schemes: Keys to understanding numerical weather prediction models*. New York, NY: Cambridge University Press. https://doi.org/10.1017/CBO9780511812590

Sun, Y., Zhong, Z., & Lu, W. (2015). Sensitivity of tropical cyclone feedback on the intensity of the western pacific subtropical high to microphysics schemes. *Journal of the Atmospheric Sciences*, *72*(4), 1346–1368. https://doi.org/10.1175/JAS-D-14-0051.1

Sun, Y., Zhong, Z., Lu, W., & Hu, Y. (2014). Why are tropical cyclone tracks over the western North Pacific sensitive to the cumulus parameterization scheme in regional climate modeling? A case study for Megi (2010). *Monthly Weather Review*, *142*(3), 1240–1249. https://doi.org/10.1175/MWR-D-13-00232.1

Thompson, G., Field, P. R., Rasmussen, R. M., & Hall, W. D. (2008). Explicit forecasts of winter precipitation using an improved bulk microphysics scheme. Part II: Implementation of a new snow parameterization. *Monthly Weather Review*, *136*(12), 5095–5115. https://doi.org/10.1175/2008MWR2387.1

Tustison, B., Harris, D., & Foufoula-Georgiou, E. (2001). Scale issues in verification of precipitation forecasts. *Journal of Geophysical Research*, *106*(D11), 11,775–11,784. https://doi.org/10.1029/2001JD900066

Wang, P., Li, J., Goldberg, M. D., Schmit, T. J., Lim, A. H. N., Li, Z., et al. (2015). Assimilation of thermodynamic information from advanced IR sounders under partially cloudy skies for regional NWP. *Journal of Geophysical Research: Atmospheres*, *120*, 5469–5484. https://doi.org/10.1002/2014JD022976

Wang, P., Li, J., Li, J., Li, Z., Schmit, T. J., & Bai, W. (2014). Advanced infrared sounder subpixel cloud detection with imagers and its impact on radiance assimilation in NWP. *Geophysical Research Letters*, *41*, 1773–1780. https://doi.org/10.1002/2013GL059067

Wang, P., Li, J., Li, Z., Lim, A. H. N., Li, J., Schmit, T. J., & Goldberg, M. D. (2017). The impact of cross-track infrared sounder (CrIS) cloud-cleared radiances on hurricane Joaquin (2015) and Matthew (2016) forecasts. *Journal of Geophysical Research: Atmospheres*, *122*, 13,201–13,218. https://doi.org/10.1002/2017JD027515

Wang, P., Li, J., Lu, B., Schmit, T. J., Lu, J., Lee, Y. K., et al. (2018). Impact of moisture information from advanced Himawari imager measurements on heavy precipitation forecasts in a regional NWP model. *Journal of Geophysical Research: Atmospheres*, *123*, 6022–6038. https://doi.org/10.1029/2017JD028012

Wang, X., Parrish, D., Kleist, D., & Whitaker, J. (2013). GSI 3DVar-based ensemble–variational hybrid data assimilation for NCEP Global Forecast System: Single-resolution experiments. *Monthly Weather Review*, *141*(11), 4098–4117. https://doi.org/10.1175/MWR-D-12-00141.1

Wang, Y., Liu, Z., Yang, S., Min, J., Chen, L., Chen, Y., & Zhang, T. (2018). Added value of assimilating Himawari-8 AHI water vapor radiances on analyses and forecasts for "7.19" severe storm over north China. *Journal of Geophysical Research: Atmospheres*, *123*(7), 3374–3394. https://doi.org/10.1002/2017JD027697

Will, M. C., Gary, J., & Miller, T. L. (2009). Impact of the assimilation of atmospheric infrared sounder radiance measurements on short-term weather forecasts. *Journal of Geophysical Research*, *114*, D18122. https://doi.org/10.1029/2008JD011626

Wu, W.-S., Purser, R. J., & Parrish, D. F. (2002). Three-dimensional variational analysis with spatially inhomogeneous covariances. *Monthly Weather Review*, *130*(12), 2905–2916. https://doi.org/10.1175/1520-0493(2002)130<2905:TDVAWS>2.0.CO;2

Yang, J., Zhang, Z., Wei, C., Lu, F., & Guo, Q. (2017). Introducing the new generation of Chinese geostationary weather satellites, Fengyun-4. *Bulletin of the American Meteorological Society*, *98*(8), 1637–1658. https://doi.org/10.1175/BAMS-D-16-0065.1

Zhang, C., & Wang, Y. (2018). Why is the simulated climatology of tropical cyclones so sensitive to the choice of cumulus parameterization scheme in the WRF model ? *Climate Dynamics*, *51*(9-10), 3613–3633. https://doi.org/10.1007/s00382-018-4099-1.

Zhang, F., Minamide, M., & Clothiaux, E. E. (2016). Potential impacts of assimilating all-sky infrared satellite radiances from GOES-R on convection-permitting analysis and prediction of tropical cyclones. *Geophysical Research Letters*, *43*, 2954–2963. https://doi.org/10.1002/2016GL068468

Zheng, J., Li, J., Schmit, T. J., Li, J., & Liu, Z. (2015). The impact of AIRS atmospheric temperature and moisture profiles on hurricane forecasts: Ike (2008) and Irene (2011). *Advances in Atmospheric Sciences*, *32*(3), 319–335. https://doi.org/10.1007/s00376-014-3162-z